Synthesis and Characterization of λ-Carrageenan Oligosaccharide-Based Nanoparticles: Applications in MRI and In Vivo Biodistribution Studies

Manon Porta-Zapata, Susana Carregal-Romero, Jennifer Saliba, Ainhize Urkola-Arsuaga, Claudia Beatriz Miranda Perez de Alejo, Iñaki Orue, Lydia Martínez-Parra, Desirè Di Silvio, Armel Descamps-Mandine, Clément Daviaud, et al.

Synthesis and Characterisation of λ-Carrageenan Oligosaccharide-Based Nanoparticles: Applications in MRI and in vivo Biodistribution Studies

Manon Porta Zapata[1], Susana Carregal-Romero[2,3,4], Jennifer Saliba[1], Ainhize Urkola-Arsuaga[2], Claudia Beatriz Miranda Perez de Alejo[2], Iñaki Orue[6], Lydia Martínez-Parra[2,5], Desirè Di Silvio[2], Armel Descamps-Mandine[7], Clément Daviaud[1], Maelenn Menard[1,10], Ameur Hamami[10], Benjamin Musnier[1], Julien Cherfan[1], Axel Codault[1], Chanez Manseur[1], Marc Jeannin[10], David Castejon[9], Ingrid Fruitier-Arnaudin[1], Jesús Ruiz-Cabello[2,3,4,8,], Hugo Groult[1,*]*

[1] Laboratoire LIENSs, UMR CNRS 7266 - La Rochelle Université, 17000 La Rochelle, France

[2] Center for Cooperative Research in Biomaterials (CIC biomaGUNE), Basque Research and Technology Alliance (BRTA), 20014 Donostia, Spain

[3] CIBER de Enfermedades Respiratorias (CIBERES), 28029 Madrid, Spain

[4] Ikerbasque, Basque Foundation for Science, 48013 Bilbao, Spain

[5] Euskal Herriko Unibertsitatea (UPV/ EHU), 20018 Donostia, Spain

[6] SGIker Medidas Magnéticas, 48940 Leioa, Spain

[7] Centre de Micro-Caractérisation Raimond Castaing, UAR3623, 31400 Toulouse, France

[8] Departamento de Química en Ciencias Farmacéuticas, Universidad Complutense de Madrid, 28040 Madrid, Spain

[9] ICTS Bioimagen Complutense (BIOIMAC), Madrid, Spain

[10] LaSIE, UMR CNRS 7356 - Université de La Rochelle, 17042 La Rochelle, France

*Corresponding authors

Hugo GROULT : Laboratoire LIENSs, 2 rue Olympe de Gouges, 17000 La Rochelle, France ; hugo.groult@univ-lr.fr, tel : +33(5).46.50.76.74

Jesús Ruiz-Cabello : CIC BiomaGUNE, Miramon Pasealekua, 182, 20014 Donostia, Gipuzkoa, Spain ; jruizcabello@cicbiomagune.es.

KEYWORDS: Oligosaccharide, λ-Carrageenan, Ferrite Nanoparticles, Magnetic Resonance Imaging, Nanomedicine

ABSTRACT

λ-type carrageenan (λ-CAR) polysaccharides remain overlooked in the preparation of medical nanoparticles (NP) due to their unsuitable rheological properties and undesired biological effects, although they can also offer advantageous properties. To overcome these obstacles, oligosaccharide derivatives (λ-COS) have been successfully applied to the synthesis of stable NP incorporating both, ferrite cores and divalent manganese (Mn^{2+}) releasable ions. The acute pro-inflammatory behaviour and anticoagulant activity of native λ-CAR were significantly reduced in the case of λ-COS and λ-COS NP, rendering possible their use for medical applications. *In vivo* MRI studies in mice showed that the λ-COS NP framework is promising for two applications. The first is partial Mn^{2+} release into the plasma to achieve intracellular Mn^{2+}-based contrast of the myocardium and imaging of the hepatobiliary system. Second, it serves as a novel sugar-based coating that confers suitable pharmacokinetic properties to NP, making it promising for further targeted therapy applications.

1. Introduction

Polysaccharides are widely used as coatings or scaffolds for the design of multifunctional nanoparticles (NP) intended for advanced biomedical applications, such as targeted, controlled drug delivery and diagnostics.[1–3] They are mostly biocompatible and can ensure a high colloidal stability to the NP, or build controlled release systems, while being easily functionalized. Furthermore, they can impart NP with additional advantageous features, such as targeting abilities or specific bioactivities.[4] However, applications often focus on particular polysaccharides varieties such as dextran[5] or chitosan[6], neglecting numerous other families with unexplored potential, such as λ-carrageenan (λ-CAR).

λ-CAR belongs to the broad family of carrageenans (CARs), a group of high-molecular-weight marine sulphated polygalactans (up to 300 kDa) derived from red algae.[7] They are characterized by long, homogeneous, linear chains of repeated disaccharide units consisting of a 1,3-linked β-D-galactopyranose (G unit), alternating with a 1,4-linked α-D-galactopyranose (D unit). Various sulphated substitutions and the presence of a 3,6 anhydro-bridge on the D unit, shape the different subtypes, the most prominent of which are kappa (κ), iota (ι), and lambda (λ). Carrageenans have been extensively used in the food[8] and cosmetic industries[9] as thickeners and texturing agents because of their unique rheological properties. They are also often cited for their specific binding of cations, making them valuable for media decontamination applications.[10–12] Furthermore, Carrageenans have been investigated for valuable bioactivities, including antitumour, antimicrobial, and immunomodulatory effects.[7,13] However, their lack of innocuousness and concomitant presence of undesirable biological properties have strongly limited their pharmacological *in vivo* applications, especially for systemic administration. Specifically, further clinical applications of λ-CAR can be limited by its viscosity and, more importantly, by its acute pro-inflammatory properties,[14–16] as illustrated by its use in a preclinical model of paw oedema in rats. In contrast, other carrageenan types exhibit a more moderate profile. Moreover, the anticoagulant properties of λ-CAR may limit its applications due to the potential risk of internal bleeding, particularly in oncological contexts where patients may have a fragile vascular system,[17] unless anticoagulant or hemocompatibility properties are specifically desired.[18] In view of these aspects, the use of carrageenans– and more specifically of the λ-type – in the field of nanomedicine is still in its early stages. Moreover, most preliminary studies have also preferred κ-CAR and ι-CAR types due to their convenient gelling properties, making them more suitable than λ-CAR for building hydrogels or self-assembled polymeric NP. Overall, the

applications tend to focus more on leveraging the rheological properties of these polysaccharides rather than their bioactivities of interest. In fact, only a few articles explicitly mention λ-CAR as a framework for biomedical NP, and these initial attempts do not mention *in vivo* experiments, as they encountered the same limitations of innocuity as described above.[19–23] Additionally, many marine polysaccharides such as Fucoidan are increasingly being studied as macromolecule-based chelates for radioisotopes or lanthanides, unlike λ-CAR which remains largely unaddressed in this domain.[24,25]

Controlled depolymerisation of λ-CAR into oligosaccharides offers a promising solution to these issues[26,27] and a way to unlock their tremendous potential as biofunctional coatings for NP. Indeed, these low-molecular-weight derivatives (typically ranging from 0.5 to 10 kDa) demonstrate significantly better physicochemical features for systemic administration than their polysaccharides counterparts, including enhanced solubility, bioavailability and reduced viscosity. Furthermore, these transformations can enhance therapeutic efficiency, discarding undesirable biological properties of polysaccharides while retaining the desired bioactivity of interest. In this regard, several promising oligosaccharides derived from λ-CAR (λ-COS) that display better druggability have already been proposed for various pathological contexts, such as oncology or infectiology.[7,28] Despite this research, surprisingly, only a few studies have reported the utilisation of oligosaccharides from carrageenans as ingredients in NP formulations, regardless of their type (κ, ι, λ).[29–33] This is especially true for λ-COS, for which, to the best of our knowledge, none have yet been described in the literature for applications in nanomedicine.

Consequently, the present study aimed to determine whether a biofunctional λ-COS framework can be applied to build novel NP-based structures and impart colloidal stability or chelation, a suitable balance of biological properties, and beneficial pharmacokinetic properties. To achieve

this, λ-COS-based NP (λ-COS NP) were prepared with extremely small encapsulated Mn-doped iron oxide (ESIONP) cores, favoured for their versatile properties as contrast agents in magnetic resonance imaging (MRI) to facilitate prospective biodistribution studies[34–36]. Next, a thorough physicochemical characterisation of this new probe was performed, revealing a second biofunctionality of the λ-COS framework, which behaves as a chelate of Mn^{2+} ions that can partially uncouple in the plasma. Importantly, the absence of common adverse bioactivities attributable to native λ-CAR was confirmed in the case of λ-COS NP. Therefore, we aimed to evaluate the input of this new sugar scaffold for NP *in vivo* applications by conducting MRI-based studies in mice at low and high fields.

2. Experimental section

2.1 Synthesis of λ-COS and basic physicochemical characterisations

A 200 mL solution of native λ-CAR (5 mg/mL) in Milli-Q water was prepared, purged with argon flow, and left to solubilise overnight. Next, 4.5 mL of H_2O_2 (30%, Merck, NJ, USA) was added, and the reactor was sealed. The mixture was then placed in a heating incubator at 60°C and stirred at 200 rpm. The depolymerisation was monitored by collecting aliquots every hour to estimate the molecular weights by size-exclusion high-performance liquid chromatography until it reached an Mn of 3.8 kDa (Mw was estimated at 7.2 KDa, yielding a dispersity of the polymer of 1.9) (corresponding to approximately 30 h of reaction).

The molecular weights of the final λ-COS were estimated by size-exclusion high-performance liquid chromatography using an Agilent 1260 Infinity II system (Santa Clara, CA, USA) composed of two analytical columns (TSK-GEL G4000PW and TSK-GEL G3000PWXL; Tosoh, Japan) coupled with a Refractive Index Detector. The samples were eluted at 25°C using a solution of $NaNO_3$ (0.1 M) at a flow rate of 0.8 $mL \cdot min^{-1}$. Molecular weights calibration was

performed using pullulan standards (from 10 to 806 kDa, Polymer Standards Service GmbH, Germany) for molecular weights higher than 10 kDa, and heparin standards (from 1200 to 5200 Da, Iduron, UK) for molecular weights below 10 kDa. The number average molecular weight (M_n), weight average molecular weight (M_w), dispersity (I), and degree of polymerisation (DP) were calculated using a previously published procedure[37] and the following equations:

$$Mn = \frac{(\sum Ni \times Mi)}{\sum Ni} \#(1)$$

$$Mw = \frac{(\sum Ni \times Mi^2)}{(\sum Ni \times Mi)} \#(2)$$

$$I = \frac{Mw}{Mn} \#(3)$$

$$DP = \frac{Mn}{Mo} \#(4)$$

where Ni is the number of moles of polymer species, Mi is the molecular weight of the polymeric species, and M_0 is the molecular weight of the monomeric unit estimated at 563.2 Da ($C_{11}H_{15}O_{20}S_3$).

The degree of sulphate was determined by Azure A colorimetric assay, as previously described.[26] Briefly, in a 96-well plate, 20 µL of sample with concentration ranging from 0 to 0.03 mg mL^{-1} was incubated at 37°C for 15 min with 200 µL of (7-aminophenothiazin-3-ylidene)-dimethylazanium chloride solution, named Azure A (Merck, NJ, USA) at 0.01 $mg \cdot mL^{-1}$. Absorbance (BMG Labtech FLUOstar Omega, Germany) was read at 630 nm, and the degree of sulfation was determined using a calibration curve built from dextran sulphate, with a known sulphur content of 18.1% (w/w) (Merck, NJ, USA). The degree of sulphate of λ-COS was 22% (±3%) w/w sulphate group.

2.2 Synthesis of λ-COS NP

First, λ-COS (40 mg) was solubilised in deionised water (1 mL). Then, 30 µmol of $MnCl_2.4H_2O$ (Sigma Aldrich >99%) was dissolved in 1 mL of 0.05M HCl and 37 µmol of $FeCl_3.6H_2O$ (Sigma Aldrich >99%) in 0.25 mL of deionised H_2O. In a 10 mL microwave tube, the λ-COS solution was added, followed by the Mn and Fe solutions. Next, 0.25 mL of hydrazine monohydrate (64-65%, Merck, NJ, USA) was carefully added before rapidly sealing the tube and placing it in the microwave unit (Discovery 2.0, CEM, NC, USA). The mixture was heated at 70 °C under magnetic stirring for 3.45 min. The reaction mixture was purified by gel filtration through a PD10 desalting column (GE Healthcare, IL, USA) using Milli-Q H_2O as the eluent.

2.3 Physico-chemical characterizations of the λ-COS NP

2.3.1 Dynamic Light Scattering measurements: The hydrodynamic diameter and ζ potential were measured in low-volume polystyrene cuvettes and folded capillary cells, respectively, using a Zetasizer Ultra (Malvern Instruments, UK). Measurements were performed in triplicate with 10 s of equilibration at 25 °C or 37 °C. The stability of the NP over time was also assessed in different media, including saline (NaCl 0.9%), Phosphate Buffer Saline (PBS, pH= 7.3, containing NaCl, KCl, Na_2HPO_4 H_2O, KH_2PO_4) and Dulbecco's modified medium (DMEM; Gibco, Fisher Scientific, NH, USA) cell culture medium was also assessed.

2.3.2 Inductively coupled-mass spectrometry (ICP-MS): 10 µL of the sample was diluted in 1 mL of 2% HNO_3 Optima™ solution and left to react overnight. The elements were dosed using an iCAP-Q (Thermo Fischer).

2.3.3 Thermogravimetric Analysis: The samples (λ-COS and λ-COS NP) were frozen overnight at -80°C and subsequently freeze-dried at room-temperature under vacuum with

COSMOS20K-Cryotec® (France). The resulting powder (5-20 mg) was then subjected to thermogravimetric analysis, heating from 20 °C to 1000 °C at a rate of 10 °C·min^{-1}, under argon flow of 20 mL·min$^{-1,}$ on a TGA/DSC3+ instrument (Mettler Toledo, OH, USA).

2.3.4 Azure A dosage: The coating was quantified using the Azure A dosage described in Section 2.1, with λ-COS as the sulphur standard.

2.3.5 Transmission electron microscopy (TEM) and dispersive X-ray spectroscopy (EDX): TEM images were obtained using a 2100F TEM (JEOL, Japan). The gun was a Schottky emitter with a high voltage of 200 kV. The grid was observed with a Gatan Rio16IS Camera in TEM mode. STEM Imaging was conducted using a JEOL ARM200 Cold FEG spherical aberration-corrected TEM equipped with a cold field emission gun operated at 200 kV. EDS spectrum and mapping were performed using an EDX SDD CENTURIO-X instrument (JEOL). All STEM images were obtained using the BF and HAADF STEM detectors. A drop of a diluted NP solution was drop-cast onto a copper grid covered with an amorphous carbon film. The grid was degassed overnight under a secondary vacuum.

2.3.6 Magnetic relaxometry: The relaxation times T_1 and T_2 were measured (in triplicates) with mq60 minispec (Bruker Biospin GmbH, 1.5T, Bruker, MA, USA) by testing 300 µL of several concentrations ranging from 2 to 20 mM (Fe + Mn) at 37 °C, with Milli-Q H_2O as the solvent. Standard T_2 Carr–Purcell Meiboom Gill and T_1 inversion-recovery spin-echo sequences were used to perform the measurements. The longitudinal (r_1) and transverse (r_2) relaxation properties were determined by plotting the $1/T_1$ and $1/T_2$ values in s^{-1} against the (Fe + Mn) concentration in mM, with Milli-Q H_2O as a blank. The relaxation values r_1 and r_2 in s^{-1}·mM^{-1} were derived from a linear fit of the resulting curve corresponding to the slope.

2.3.7 Raman and infrared spectroscopy: Raman spectra were acquired on freeze-dried samples (same protocol as described in section 2.3.3) using a Jobin Yvon High- Resolution Raman spectrometer (LabRAM HR-Evo, LabRAM, UK) equipped with a microscope (Olympus BX 41) and a Peltier- based cooled charge- coupled device detector (CCD). A laser diode was used as the excitation source at a wavelength of 532 nm. Spectra were recorded using the acquisition LabSpec software at RT, with a resolution of 0.4 cm^{-1}. Infrared spectra were acquired using a UATR Two FT-IR spectrometer, LiTaO3, with an MIR detector (PerkinElmer, MA, USA), from 4000 to 450 cm^{-1} with 64 scans, a nominal resolution of 2 $cm^{-1,}$ and a scan speed of 0.2 $cm \cdot s^{-1}$. Curves were processed using LabSpec and baseline was corrected.

2.3.8 X-ray photoelectron spectroscopy (XPS): XPS experiments were performed using a Versaprobe III Physical Electronics (ULVAC, MA, USA) spectrometer with a monochromatic X-ray source (Al Kα line of 1487 eV) calibrated using the $3d_{5/2}$ line of Ag (368.3 eV). The samples were mounted on nonconductive tape. Z-alignment was performed to determine the optimal sample height before each measurement. Argon Ion Gun and E-neutralizer were used for charge neutralization. Elemental quantification was performed on a survey scan with a step energy of 0.5 eV and pass energy of 224 eV. High-resolution regions were acquired with a step energy of 0.05 eV, pass energy of 55 eV and time per step of 50 ms. Data were analysed using CasaXPS software (2.3.25 PR 1.0). The spectra were calibrated according to the sp^3 C-C peak, and the BE was fixed at 284.8 eV.

2.4 Bioactivities evaluations and cell culture experiments

2.4.1 Cell culture conditions: Cell lines were purchased from ATCC (American Type Culture Collection, France), and human embryonic kidney cells (HEK293) and murine macrophages (RAW264.7) were chosen as models for healthy cells and immune cells, respectively. Cells were

cultured in DMEM supplemented with 10% decomplemented FBS and 1% penicillin/streptomycin (both from Gibco, Thermo Fisher Scientific, MA, USA). All cell lines were maintained at 37 °C in a humidified atmosphere containing 5% CO_2, and were mycoplasma-free (MycoAlert Mycoplasma Detection Kit).

2.4.2 Evaluation of inflammatory activity: In a 24-well plate, $1.8 \cdot 10^5$ cells·well^{-1} were treated with different samples (λ-CAR, λ-COS, or λ-COS NP) at a concentration of λ-CAR or λ-COS (assessed by Azure A dosage for the λ-COS NP) fixed at 100 µg·mL^{-1} for 24 h of incubation. IL-6 and TNF-α levels in the cell supernatants were quantified using ELISA Development Kits (PeproTech), according to the manufacturer's instructions.

2.4.3 Anticoagulant Xa/IIa inhibitory activity: The inhibition of Xa and IIa have been assessed by a colorimetric assay using anti-thrombin (ATIII), Thrombin (IIa), Factor Xa and the corresponding chromogenic substrates Xa/IIa (STACHROM® AT III and STACHROM® HEPARIN kits from Stago, France). In brief, 25 µL of the sample (λ-CAR, λ-COS, or λ-COS NP, performed in triplicate) or Milli-Q H_2O (as blank) were mixed in a 96-well plate with 25 µL of ATIII (0.625 µg·µL^{-1} in deionised water) and incubated at 37 °C for 2 min. Then, 25 µL of Factor Xa or Thrombin IIa (11.25 nkat·mL^{-1} in deionised water) was added and incubated for 2 min at 37°C. Finally, 25 µL of the corresponding chromogenic substrate (Xa or IIa) was introduced, and the absorbance was read at 405 nm in kinetic mode for 4 min (BMG Labtech FLUOstar Omega). The initial velocity, corresponding to the slope of the absorbance with respect to time in h$^{-1,}$ was calculated. The Inhibition percentages were calculated using the following equation:

$$Inhibition(\%) = \frac{Vi(blank) - Vi(sample)}{Vi(blank)} \times 100 \quad \#(5)$$

where $Vi(blank)$ and $Vi(sample)$ are the initial velocities of the blank and sample, respectively. Data were processed with Graph-Pad Prism 8 and IC_{50} were calculated by first normalizing the values and fitting to the model "absolute IC_{50}," except for IIa inhibition of the λ-COS NP because the values did not follow an IC_{50} inhibition curve.

2.4.4 Metabolic Activity assay: In a 96-well plate, cells were seeded at 10^4 cells·well^{-1} in 200 µL of adequate cell culture medium and incubated for 24 h. The medium was then replaced with 200 µL of fresh medium containing native carrageenan, λ-COS, or λ-COS NP at 0, 10, 50, 100 or 200 µg·mL^{-1}. After 24 h of exposure, 25 µL of 3-(4, 5-dimethylthiazol-2-yl)-2, 5-diphenyl tetrazolium bromide (MTT) solution was added to each well, followed by 3 h of incubation. The supernatant was then removed and replaced with 100 µL of DMSO to dissolve the formed formazan crystals, and the absorbance was read at 540 nm. Viability was calculated using the following equation:

$$Viability\ (\%) = \frac{Average\ Abs(sample)}{Average\ Abs(control)} \times 100\ \#(6)$$

2.4.5 Cellular uptake of nanoparticles: Cells were seeded in 24-well plates (10^5 cells·well^{-1}). After 24 h, cells were treated with 100 µg·mL^{-1} native carrageenan, λ-COS, or λ-COS NP λ-COS NP. After 24 h of incubation, λ-COS NP internalisation was qualitatively assessed by microscopic observation (ZEISS microscope, Axio Observer Z9, magnification: × 10, ZEISS, Germany) using a Prussian blue nuclear fast red staining kit (Abcam®). Images were constructed using Fiji software.

2.4.6 Statistical analysis: One-way or Two-way analysis of variance (ANOVA) and t-tests were performed to identify significant differences between the control and experimental groups. All experimental data were obtained from at least three independent experiments. All statistical

analyses were performed using GraphPad Prism version 8 for Windows. A probability (p) value <0.05 was considered statistically significant.

2.5 In vivo experiments

2.5.1 Animal ethics: All animal experiments were performed in accordance with the Spanish policy for animal protection (RD53/2013), which meets the requirements of Directive 2010/63/UE. The 7T procedures were approved by the Ethical Committee of the CIC biomaGUNE and authorised by the local authorities (PRO-AES-SS-225).

2.5.2 MRI 7-Tesla and 1-Tesla in vivo imaging: The λ-COS NP solution was concentrated with a 30 kDa filtration unit (Amicon®, Merck) for 10 min in a centrifuge (Minispin®, Eppendorf, Germany) at 7000 rpm, resuspended in saline (NaCl 0.9%), placed in an ultrasound bath for 10 min, and filtered through a 0.22 μm filter (Merck Millipore). Fifty to one hundred microlitres of this solution were intravenously injected into 7-week-old BALB/cJRj mice (Janvier Lab, France). Biodistribution studies were assessed under two distinct magnetic field conditions.

MRI 1 Tesla was performed at the ICTS-BioImaC of the Universidad Complutense, node of the ICTS ReDIB (https://www.redib.net/), using a 1 Tesla benchtop MRI scanner (ICON 1 T-MRI; Bruker BioSpin GmbH, Ettlingen, Germany). The system consisted of a 1 Tesla permanent magnet with a gradient system capable of supplying a gradient strength of 450 $mT \cdot m^{-1}$. A solenoid mouse-body RF coil was used. Animals (6-week-old female Balb/c mice) were anaesthetised using 2% isoflurane (IsoFlo, Zoetis, NJ, USA). The main MRI experiment consisted of three-dimensional T_1 weighted images used to monitor the evolution of contrast enhancements, before and after λ-COS NP intravenous injection. The isotropic T_1 weighted experiments (0.5 × 0.5 × 0.5 mm) were acquired using a gradient echo sequence with a repetition

time of 20.3 ms, an echo time of 2.0 ms and flip angle of 20 °. The total acquisition time was 6 min.

Other parts of the experiments were performed at the ICTS-CIC BiomaGUNE on a 7 Tesla Bruker Biospec 70/30 USR MRI system (Bruker Biospin GmbH, Ettlingen, Germany), interfaced with an AVANCE III console. A BGA12 imaging gradient (maximum gradient strength 400 $MT \cdot m^{-1}$) system, with a 40 mm diameter quadrature volume resonator, was used for MRI data acquisition. Anaesthesia was induced using 4-5% isoflurane in 30% oxygen and maintained at 1−2% isoflurane throughout the experiment. The animals were positioned in a customised 3D-printed bed equipped with a head holder and maintained at 37 °C using heated air pumped through an MRI-compatible system, interfaced with Monitoring and Gating Model 1030 (SA instruments, NC, USA). Anal temperature control and respiration (monitored through a respiratory pad) were recorded throughout the experiment. Anatomical images of the abdomen were acquired with a Bruker gradient echo FLASH sequence using the following parameters: TE 4 ms, respiration synchronised (TR 600 ms), flip angle 30 °, 2 averages, 256 x 256 points, a Field of View of 4 cm x 4 cm and 12 non-contiguous slices with a slice thickness of 1.0 mm. Quantification was performed using T_2 maps to facilitate comparison on different days of the experiment. T_2 maps were obtained using a multislice spin-echo (MSME) sequence. The TE values varied in 20 steps, ranging from 8 ms to 160 ms, and were synchronised with respiration (TR 4000 ms). T_2 maps were created with a customised python-based script to adjust and calculate the maps and were analysed using the ITK-SNAP software. Images were acquired before injection and between 30 min, 2 h and 24 h after injection of the NP solution.

2.5.3 Ex vivo analysis. Histopathological analyses were performed by fixing the tissues in Formalin 4%. This was followed by a series of washes with ethanol (50%, 75%, and 100%

concentrations) and xylene and then embedded in paraffin. Subsequently, the tissues were sectioned using a microtome. Two different staining methods were applied: i) haematoxylin and eosin staining to observe the integrity of the tissues, and ii) Prussian blue staining to highlight the presence of iron in the cells. Final observations were performed using a confocal microscope (Zeiss LSM 880 Airyscan). Organs were freeze-dried according the procedure described in section 2.3.3. using Christ®, Alpha 2-4 LSCplus (Germany). The Mn and Fe contents in the freeze-dried organs were quantified after digestion in a 2% HNO_3 Optima Microwave Digestion System Speedwave XPERT (Berghof SpeedWave Xpert, Germany) using an established protocol for meat digestion. The elements were dosed as described in the ICP-MS section.

2.6 Data curation

All data and graphs were processed using Excel (Microsoft, USA) or GraphPad Prism (release 8 for Windows), and the schemes were implemented using Biorender (Canada) and PowerPoint (Microsoft, USA).

3. Results and discussion

3.1 Synthesis of λ-COS NP

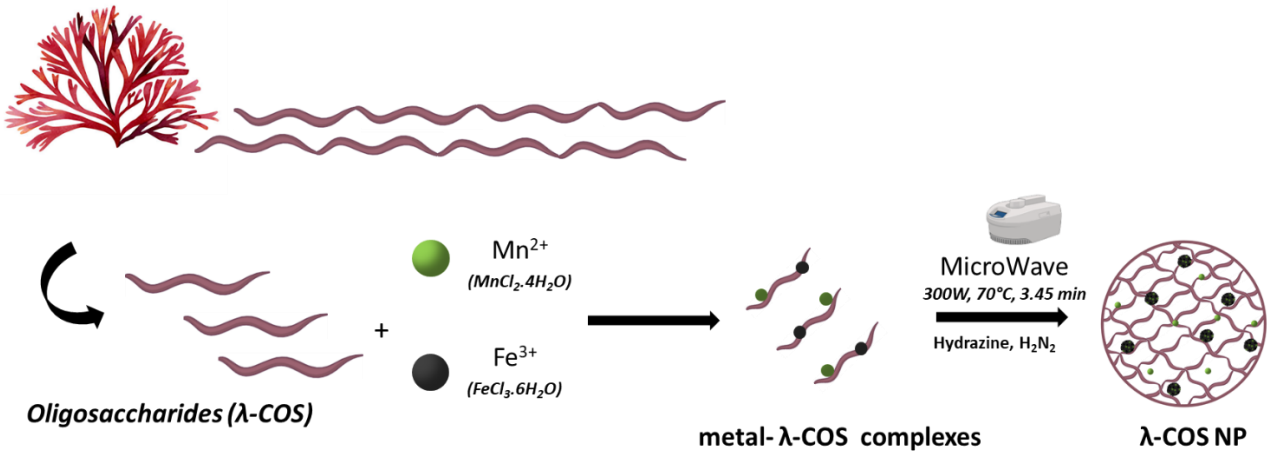

Figure 1. Synthesis of λ-COS NP. λ-COS was prepared by a radical-based depolymerisation method and next λ-COS NP were prepared using a two-step method: 1) Mn + Fe λ-COS coordination complex and then in situ 2) crystal growth of ESIONP using reductive thermal treatment.

λ-COS was obtained from native λ-CAR polysaccharides using a previously published, H_2O_2-based radical depolymerisation method.[38] The basic physicochemical parameters of λ-COS include an M_n of 3.8 KDa with a dispersity of the polymer of 1.9 (measured by size-exclusion high-performance liquid chromatography with spectra displayed in **Figure S1**), and a degree of sulphate of 22 (± 3) % (measured by a colorimetric quantification assay). λ-COS-based hybrid NP embedding free Mn^{2+} ions and extremely small iron oxide (ESIONP) cores, referred to here as **λ-COS NP**, were prepared by a one-pot synthesis divided into two steps (**Figure 1**).[39] First, manganese dichloride tetrahydrate ($MnCl_2.4H_2O$) and iron trichloride hexahydrate ($FeCl_3.6H_2O$) precursors (molar ratio of 1:1.2, Mn) were added together to a λ-COS solution (40 $mg{\cdot}ml^{-1}$), forming a water soluble metals- λ-COS coordination complex. The ability of Mn^{2+} and Fe^{3+} to bind with carrageenans polysaccharides through interactions between the metal ions and the negatively charged sulfate ($-SO3^-$) groups[40–42], and to a lesser extent hydroxyl (-OH) groups[19,40,43], has already been documented in several articles. However, this is the first time such effects have been observed for OS. Dynamic light scattering measurements showed no aggregation or self-assembled NP at this stage, most likely due to the low-molecular-weight of oligosaccharides (limiting the number of available binding sites for crosslinking compared to native PS). And yet, effectiveness of the water-soluble metals- λ-COS coordination complex was corroborated by other experiments (**Figure S2**). First, an FTIR analysis of the free λ-COS and the metals- λ-COS coordination complex was carried out. Participation of hydroxyl (−OH)

groups in the coordination of metals was revealed by a broadening of the band in the complex's spectra, compared to the one obtained from the free λ-COS. A clear down-shift of the asymmetric S=0 stretch from ~1220 cm^{-1} to ~1209 cm^{-1} was detected in the complex's spectra, confirming the participation of sulphate groups in the stabilisation of the metal ions. Moreover, ζ-potential measurements of the λ-COS solution showed a slight shift from -13.9 to -11.3 mV upon addition of the metal salts. Finally, the peak at 573 cm^{-1}, characteristic of λ-COS skeleton's additional features, displayed a higher intensity after complexation. This could be compatible with the presence of an additional band corresponding to the Metal-oxygen (M-O) bond vibrations, which - shifted from 533 cm^{-1} to the 573 cm^{-1} peak, when metal salts were alone. Next, UV-visible analyses were performed to complete the picture and higher absorbances were observed in the UV region (200-300 nm^{-1}) of the metals- λ-COS coordination complex's spectra, compared to those of free metals and λ-COS taken alone, indicating a ligand-to-metal charge transfer consistent with a complex formation (**Figure S2**). [44]

In the second step, using a previously developed method for preparing various natural PS- and OS-coated ESIONP[45,46], hydrazine was added *in situ*, followed by a quick, mild thermal treatment (70°C for 3 min 45 s). This process induced the rapid formation of intermediate iron hydroxides, as well as the partial reduction of Fe^{3+} into Fe^{2+}, facilitating the nucleation and growth of crystalline ESIONP cores, which in turn drives a nano-sized λ-COS matrix assembly as a stabilizer. The final hydrodynamic diameter (HD) of λ-COS NP, measured by dynamic light scattering, was 79 ± 2 nm. The size range of 50 -150 nm is generally considered suitable for achieving prolonged circulation time (avoiding rapid clearance by the renal and mononuclear phagocyte systems), efficient cellular uptake, and passive targeting, particularly in antitumour applications.[47] The ζ-potential of λ-COS NP, measured at physiological pH, was highly negative

at -21.0 ± 0.8 mV due to the presence of negatively charged sulphate groups in the λ-COS framework. This strong negative value is expected to provide effective electrostatic stabilisation, which is crucial for preventing aggregation and ensuring colloidal stability.[48] A control reaction, consisting in the single addition of iron precursor without Mn^{2+}, resulted in NP with a larger HD of 215 ± 3 nm and embedded low-quality amorphous ESIONP cores (data not shown), indicating the importance of Mn^{2+} addition in modulating the kinetics of intermediate iron hydroxide formation. By competing with the Fe binding sites, Mn^{2+} probably slowed the burst nucleation (i.e. iron hydroxides forming too rapidly which prevent the ordered crystal growth) and an iron hydroxide-induced higher aggregation of the λ-COS matrix.

3.2 Advanced characterization of λ-COS NP

To further describe the final λ-COS NP, final amounts of Mn and Fe in the structure were quantified by ICP-MS (**Figure S3**). The final loading efficiencies of the metals in the NP were approximately 20 % of the initial amounts introduced in both cases. Subsequently, the λ-COS NP were resuspended in an aqueous solution of Zn^{2+} at 2.5 mM, as Zn^{2+} can quantitatively substitute divalent cations that are complexed within organic structures.[49] After ultracentrifugation of the solution using a 3 kDa cut-off, Mn and Fe were quantified in the filtrate. Results showed no detectable Fe, indicating that all the iron complexed at the 1st step had reacted and was finally contained within the encapsulated ESIONP cores. On the other hand, 90% of the total Mn was released, which corresponds to the complexed Mn inside the λ-COS NP, while the remaining 10 % were Mn that diffused in ESIONP cores during crystal growth in the 2nd step of the reaction. Consequently, the ESIONP composition could be refined to the following stoichiometry: $Mn_{0.2}Fe_{2.8}O_4$ and will now be referred to as **ferrite cores**.

As shown in **Figure 2A** and **S4**, large field-of-view TEM images in bright-field and dark-field modes highlighted these inorganic cores of round-like shape arranged in bunches among the λ-COS NP organic matrix. Core diameters computed from these images exhibited a distribution of 2.6 ± 0.4 nm on average (***Figure 2A***). This, in relation to the HD of 79 ± 2 nm, suggests the presence of a cohesive λ-COS matrix encapsulating multiple cores, rather than a simple surface coating. EDS maps from the TEM image also indicated colocalization between the Fe atoms and the observed cores, while Mn atoms were distributed more largely due to the Mn population complexed in the λ-COS framework (**Figures S5** and **S6**), in addition to the Mn doping found in the cores. Additional HRTEM microscopy analysis revealed their good crystallinity, as confirmed by the numerous lattice fringes that were detectable (**Figure 2B**). The measured d-lattice spacings from the SAED patterns were in good agreement with the ones found for spinel manganese ferrite, including 2.38, 2.14, 1.46 and 1.17 Å for the (220), (311), (400) and (331) planes, respectively (**Figure S7**).[50,51] Finally, Raman spectroscopy is a valuable tool for characterizing the crystallographic structure of these encapsulated ferrite cores.[52,53] In the spinel arrangement, the oxygen anions are packed in a face-centred cubic structure, forming a basic structure, and tetrahedral (Td) and octahedral (Oh) sites can be occupied by metallic ions to form normal, mixed, or inverse structures. Indeed, in normal spinel structures, divalent ions reside in the Td sites, while trivalent ions are in the Oh sites. In the inverse structure, however, such as in magnetite (Fe_30_4), the trivalent ions are equally distributed between the Td and Oh sites, with divalent ions in the Oh sites. Since Mn^{2+} can occupy both Td and Oh sites, Mn doped-Fe_3O_4 typically build mixed structures with varying degrees of inversion, depending on the ratio of Mn substitution, the type of synthesis, or the particle size. [52,54,55] The pattern obtained with λ=532 nm excitation closely matched this scenario, displaying an intense peak at 614 cm^{-1}, in particular.

This is attributed to the A1g mode and corresponds to the Fe^{3+}-O stretch vibration in the Td sites, with shifts due to the local distortion induced by the Mn substitution (**Figure 2C**).[54] The broadening of this band towards higher wavenumbers specified the vibration modes of other cations in the Td sites, prone to be Fe^{2+} or Mn^{2+} ions and indicative of partial inversion in the spinel. The other peaks below 600 cm^{-1} are associated with the vibration between the cations located at the Oh sites and oxygen groups. Accordingly, the bands observed at ~ 320 cm^{-1} and ~ 450 cm^{-1} can be considered as one of the Eg (symmetric bending) and T2g (antisymmetric bending) modes of Fe^{3+}, with shifts that are more consistent with the normal characteristics of the spinel. [52,54,55] However, the broadening of the T2g bands can be attributed to the presence of other types of ions (Mn^{2+} or Fe^{2+}) at the Oh sites.

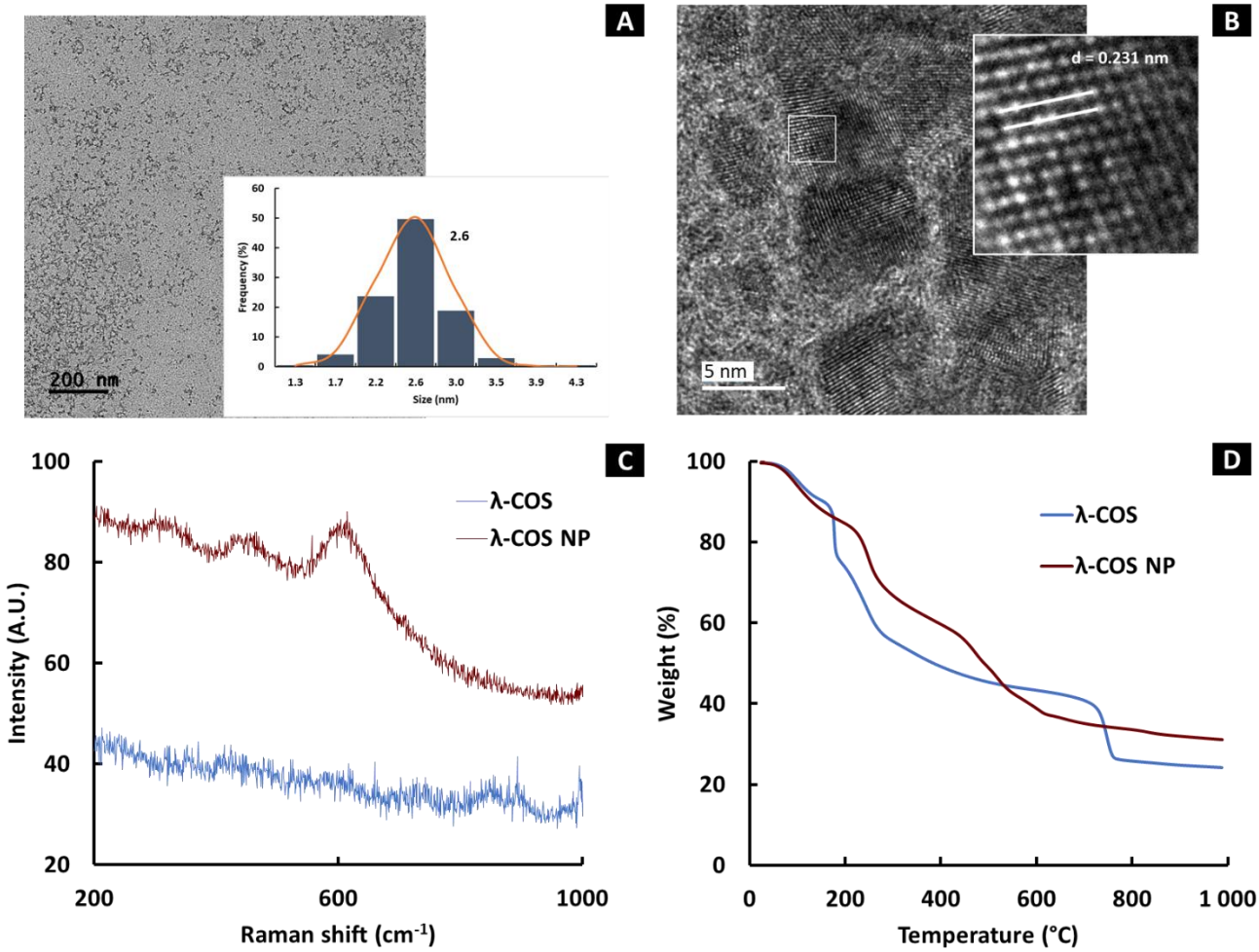

Figure 2. Characterisation of λ-COS NP. (A) TEM images and size distribution, (B) HRTEM and d-spacing and (C) Raman spectra at 785 nm of the encapsulated ferrite cores. (D) Thermogravimetric analysis curves of the λ-COS and λ-COS NP.

Next, the proportions of the different elements constituting the λ-COS NP were investigated. Colorimetric quantification of the sugar-based coating[26], when compared to ICP-MS analysis of the overall metal ions, yielded a final λ-COS to metal (Fe + Mn) w/w ratio of 11.1. A thermogravimetric analysis was also performed to characterise the balance between organic coating and ferrite cores amounts. As shown in **Figure 2D,** the degradation of λ-COS NP was divided into three stages: an initial loss of up to approximately 200°C, corresponding to the

evaporation of bound water; a second step from 200 to 600°C, attributed to the degradation of the organic coating; and finally, a plateau representing the mass retention of the ash content and metal oxide formation that accounted for 31.1 % of the weight. A comparison of this plateau with that obtained from the thermogravimetric analysis of the free λ-COS (24.2% remaining weight) indicates that the encapsulated ferrite cores of λ-COS NP accounted for approximately 7 % of the weight of the sample. The weight ratio of λ-COS/(Fe + Mn) w/w (13.3) obtained in this experiment was consistent with the ratio estimated earlier (11.1). Next, multiangle dynamic light scattering measurements were used to estimate NP concentration in the solution. Based on previous data obtained and the M_w of λ-COS, several parameters were estimated, namely, the average number of oligosaccharide chains, ferrite cores and complexed Mn per total NP, to determine whether the orders of magnitude were consistent with the described system (**Table S8)**. The calculations indicated that a single NP contained approximately 1.3×10^6 λ-COS chains, 2.7×10^4 ferrite cores, and 5.7×10^6 Mn atoms, which aligns reasonably with earlier descriptions of the NP. More explicitly, these values correspond to roughly 4 Mn atoms per λ-COS chain and about 50 λ-COS chains per ferrite core (equating to a density of 2.34 chains/nm² of ferrite cores' surface), in good agreement with previous data.[40,45]

3.3 XPS and FTIR characterisation of λ-COS NP

To complete the chemical characterisation of λ-COS NP, XPS analysis was performed on both λ-COS NP and λ-COS (**Figure 3A-E** and **Figure S9**). The organic elements and chemical functional groups expected in λ-COS/CAR were retrieved from the NP spectra with C, O, S, and Na as the counter ions (**Figure 3A**). A minor proportion of nitrogen (3.7 %) was detected in the free λ-COS and in the NP samples, which was unexpected considering the theoretical chemical structure of the sugar. The C/S ratio in the λ-COS NP sample (3.8) was significantly lower than

that in the free λ-COS coating (11.6), indicating a partial desulphation during the NP synthesis. Indeed, in the C 1s spectra, deconvolution attributed to C-O also decreased (**Figure S9**) and that might correspond to this desulphation.[56] The asymmetric O 1s peak in the λ-COS NP XPS spectra can be deconvoluted into various contributions (**Figure 3B**). The lowest binding energy (530.5 eV) is commonly associated with metal-oxygen bonds, while the higher contributions (up to 531 eV) correspond to the oxygen bonds present in the saccharidic coatings (C-O -SO^{3-}, C=O). It is interesting to note a shift in the O_{ads} binding energy towards higher values, compared to the spectra of the free λ-COS, indicative of the change in their neighbouring environment resulting from the participation of the hydroxyl and sulphate groups in metal stabilisation.[56,57] In addition, adsorbed water in the free λ-COS sample, detected through the signal at 536-537 eV, was no longer present in the NP sample. Regarding the metallic ions, two peaks were observed at 642 and 654 eV for Mn, corresponding to Mn $2p_{3/2}$ and Mn $2p_{1/2}$, respectively (**Figure 3C**). The presence of the satellite peak at 645 eV (shake-up) confirmed the presence of paramagnetic Mn^{2+} complexed in the nanoarchitecture.[58] Deconvolution of the Mn $2p_{3/2}$ could indicate the minor presence of other higher oxidation forms of Mn (+ III or + IV).[59] , and yet signals from the Mn 3s were split into two peaks at 83.76 and 89.85 eV, giving a ΔE of 6.1 eV (**Figure 3D**). This ΔE value indicated a prevalent Mn^{2+} oxidation state, as reported in the MnO XPS spectra.[59] On the other hand, analysis of Fe signals is entirely related to the ferrite cores. This can be seen from **Figure 3E:** the two main asymmetric peaks, Fe $2p_{1/2}$ and Fe $2p_{3/2}$, with binding energies at 710.5 and 723.8 eV, giving a doublet spacing of 13.3 eV. The presence of their respective satellite peaks at approximately 715 and 728 eV reveals that Fe^{3+} is the main oxidation state present in the core, even if subtle shoulder can indicate the minor presence of Fe^{2+}. Several contributions to Fe $2p_{3/2}$ might be detected, potentially reflecting the three different environments of the Fe^{3+}

ions. The apparent shift towards the higher binding energy at 711 eV suggests the predominance of Oh site occupation and hydroxyl group binding, which is consistent with the Raman results (**Figure 2C**).

A

	C (at%)	O (at%)	N (at%)	Na (at%)	Ca (at%)	S (at%)	K (at%)	Fe (at%)	Mn (at%)
λ-COS	28.5	52	3.7	5.5	2.7	7.4	0.2	-	-
λ-COS NP	43.1	46.3	2.2	1	-	3.7	-	1.4	2.3

B

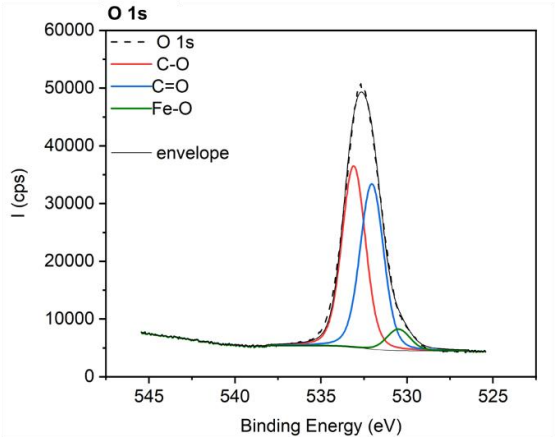

C

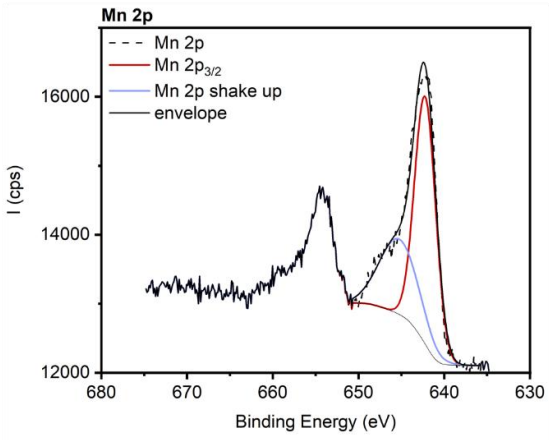

D

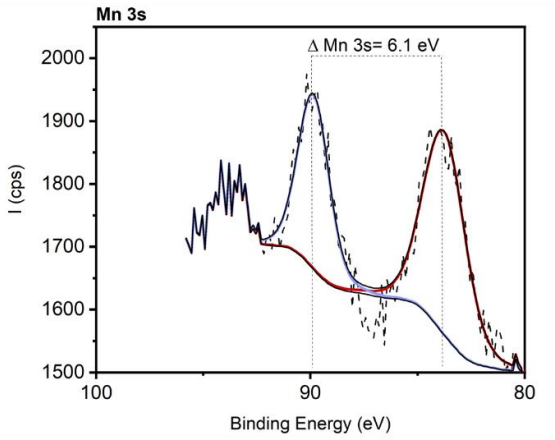

E

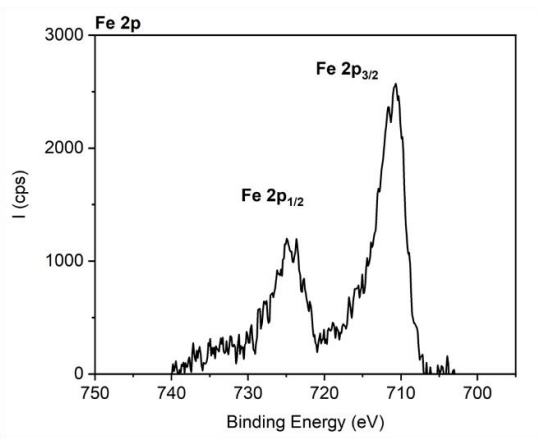

F

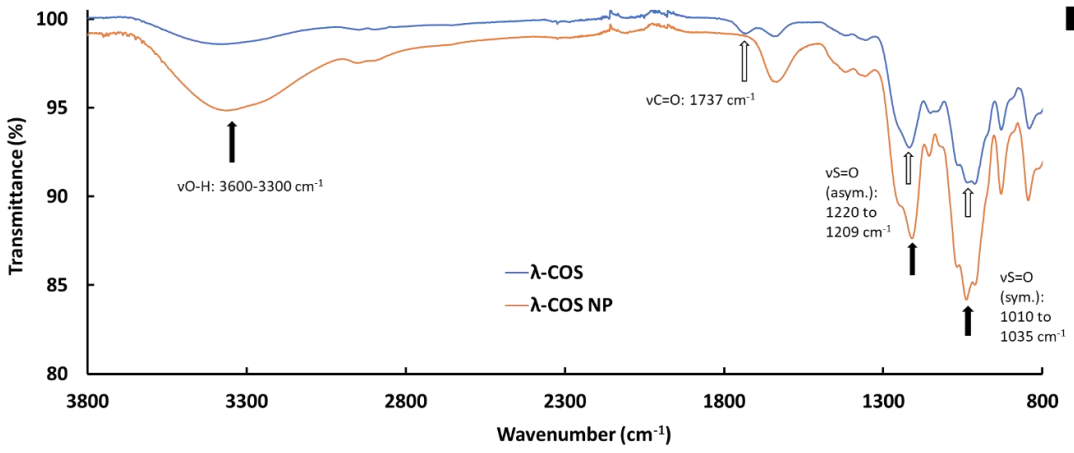

Figure 3. Coating characterisations; (A) Table of atomic quantification, XPS spectra of (B) O1s, (C) Mn 2p, (D) Mn 3s, (E) Fe 2p and (F) FT-IR spectra of λ-COS NP.

Next, FTIR analyses were performed in an attempt to confirm and decipher the chemical groups of λ-COS that interact with the different elements (Mn^{2+}, ferrite cores) in the final NP (**Figure 3F**). The main peaks corresponding to the λ-COS's functional groups were successfully retrieved in the two spectra. The band corresponding to the hydroxyl groups (3600-3300 cm^{-1}) was slightly broader in the λ-COS NP spectra, confirming their participation in the structure stabilisation. The S=O asymmetric stretch shifted from 1220 cm^{-1} (free λ-COS spectra) to 1209 cm^{-1} in the final NP, together with a change in relative intensities of the S=O symmetric stretch (1010-1035 cm^{-1}). This is indicative, once again, of the importance of sulphate groups in the coordination of the Mn^{2+} and ferrite cores. Glycosidic linkage (1070 cm^{-1}), anhydro-galactose ring (930 cm^{-1}) and C-O-S peaks (845 cm^{-1}) remained unchanged. To be noted, the signal at 1737 cm^{-1} in the λ-COS spectra, which can be attributed to the open reducing ends exposing an aldehyde group, were not retrieved in the one of λ-COS NP. As this change was not detected in the metals- λ-COS coordination complex's spectra displayed previously, it could indicate an additional contribution of the reducing ends towards the ferrite core's stabilisation.

3.4 Magnetic characterization of λ-COS NP

All these structural features strongly influence the magnetic properties of the λ-COS NP. To study them, magnetometric measurements were performed. Firstly, the magnetisation, according to magnetic fields (M(H)) recorded at 10 K of the lyophilised samples, revealed that the sample was not completely saturated in the field range used (4 $MA \cdot m^{-1}$), thus confirming the presence of complexed paramagnetic ions and/or very fine NP (**Figure 4A**).[60] Previous literature for extremely small ferrites often reports the presence of a magnetic dead layer in which spin canting

and surface magnetic disorders profoundly impact saturation magnetisation by reducing the net magnetic alignment.[61] It was observed that, up to 150 K, the M(H) curves displayed full paramagnetic behaviour (**Figure S10**). Further to this, the temperature dependence of the magnetisation was measured with the ZFC-FC procedure from 2 to 270 K under a magnetic field of 8 $kA \cdot m^{-1}$ (**Figure 4B**). The derivative of the temperature difference between the FC and ZFC branches provided a very small experimental blocking temperature (Tb) of 3 K (graph not shown). Next, all ZFC-FC and M(H) curves were fitted to a model of non-interacting particles (labelled "Total Fit" in **Figure 4A** and **4B**). Both, ZFC-FC and M(H) at 10 K curves fit quite well to this model by assuming a superposition of two distributions of populations (identified as dist1 and dist2, respectively), given by two different supermoments of approximately 150 Bohr magnetons (μ_B) (1.3 %) and 4 μ_B (98.7%). In this case, the small bump, or relative maximum of the ZFC-FC curve, located at 5 K is due to the small fraction of "dist 1" 150 μ_B NP. From the M(H) fit in **Figure 4B**, the saturation magnetisation (Ms) of this NP superparamagnetic population can be estimated, which is approximately 26 $A \cdot m^2 \cdot kg^{-1}$ (without correction of the organic content). Also, whatever the value for the spontaneous magnetisation of the particles used, it was possible to estimate the magnetic size of the different objects in the two populations. Taking M = 400 $kA \cdot m^{-1}$, the first population magnetic size was estimated to be approximately 2.4 nm and the second was approximately 0.75 nm. For the first, this result matches well with the magnetic core diameter calculated for the ferrite cores population from TEM images (2.6 nm), and for the second, it reinforces the previous indications about the presence of complexed Mn in the λ-COS matrix.

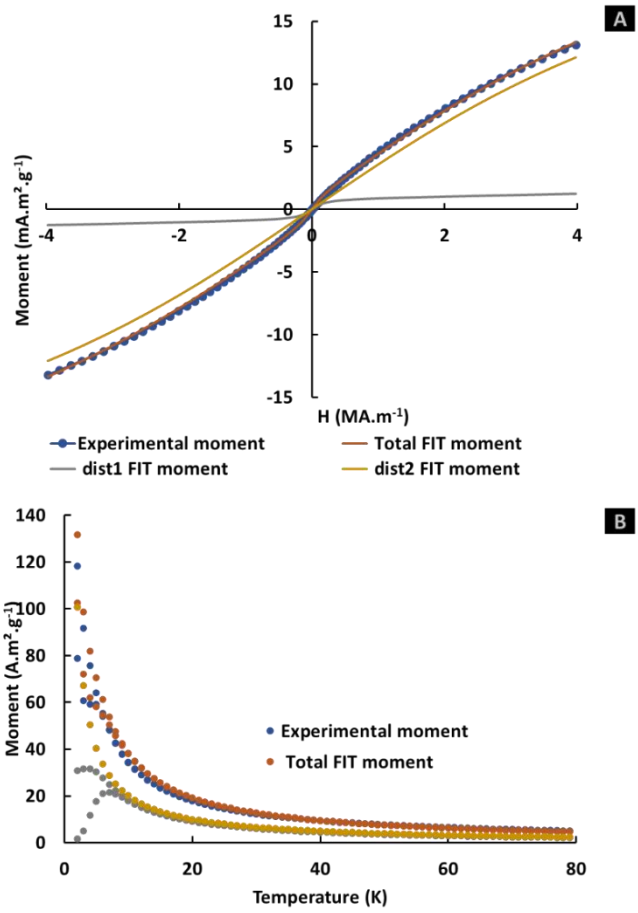

Figure 4. Magnetic characterisation of λ-COS NP; (A) magnetisation curve M(H) at 10 K (experimental moment) and (B) ZFC-FC curves (experimental moment) with theoretical fitting (Total FIT) made from two distributions of populations (dist1 and dist2).

To assess the potential of the λ-COS NP as MRI CA, its relaxometric properties were measured at 37°C using a 1.5 Tesla relaxometer. Additionally, serial dilutions of phantoms in 1 Tesla and 7 Tesla MRI scanners were also performed to study their response in low-middle and high magnetic fields, and both were used for upcoming *in vivo* studies (**Figure S11**). At 1 Tesla, the relaxivity values r_1 and r_2 measured from the phantoms were 2 and 14.6 $mM^{-1} \cdot s^{-1}$, respectively. These results were comparable to those obtained using the relaxometer with a close magnetic field of 1.5 Tesla: r_1 of 2.47 ± 0.01 $mM^{-1} \cdot s^{-1}$ and r_2 of 18.2 ± 0.2 $mM^{-1} \cdot s^{-1}$. At 7 Tesla,

the r_1 value computed from the signals remained roughly similar (2.3 $mM^{-1} \cdot s^{-1}$), while r_2 value was much higher 52.7 $mM^{-1} \cdot s^{-1}$, indicating that λ-COS NP are more appropriate for T_2-weighted imaging at this high field. Explanations could lie in the fact that, at high fields, the T_1 reduction induced by complexed Mn ions in the NP frameworks is not strongly enhanced compared to low fields, while the T_2 contrast arising from the ferrite cores, also present in the NP, is highly favoured.

3.5 Stability of λ-COS NP and controlled release of Mn in serum

The high mass ratio of the coating to the nanoparticle core, combined with the highly negative ζ potential, confers high colloidal stability to the NP at physiological pH. To go further, the stability of λ-COS NP across a pH range of 3.5–9.5 was also studied by measuring the HD and ζ potentials (**Figure 5A** and **5B**). The HD remained almost constant, ranging between 71 and 80 nm (as measured by recording the signal intensity which is the most sensitive criterion used to detect the eventual presence of aggregates), with the minimum observed at a pH of 7-7.3, corresponding to the typical physiological pH. The ζ potential remained stable at approximately − -30 mV until pH 8.5, beyond which it decreased to -41 mV under basic conditions. A similar curve pattern was observed for the λ-COS alone, with a drop-off at a pH of 8.5 which is coherent with the previous literature.[62] The stability of the NP over time in various media, relevant to future experiments, was also assessed by HD monitoring (**Figure 5C**). In DMEM, a small increase in HD was observed, likely due to the presence of proteins that crosslink or adsorb onto the NP surface. However, the NP remained stable over four days, indicating the suitability of this medium for studying the effects of NP in cell-based studies. The results also showed that the HD was similar in saline (NaCl 0.9%) and Milli-Q H_2O, and it remained generally stable over four days. In contrast, aggregation and destabilisation of the NP occurred in PBS, likely due to the

high salt content. Therefore, saline was identified as an appropriate isosmotic buffer for further intravenous administration in *in vivo* mouse studies.[39,63]

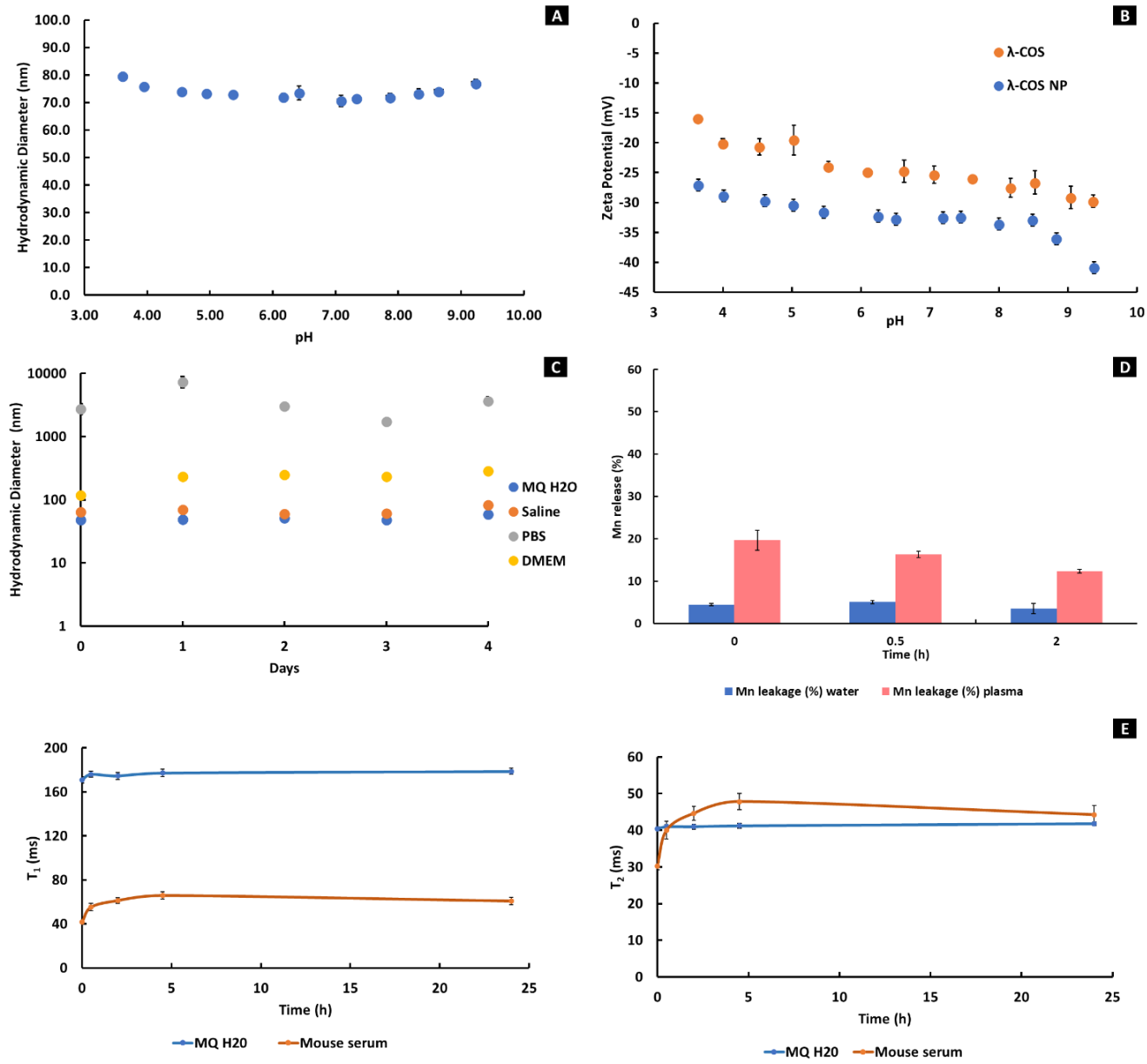

Figure 5. Stability of the λ-COS NP in solution; (A) HD measured by dynamic light scattering (Z-Average values) values according to the pH (between 3.5 and 9.5), (B) ζ potential according to the pH (between 3.5 and 9.5), (C) HD measured by dynamic light scattering (Z-Average values) of the λ-COS NP in different media (mQ H_2O, saline, PBS and DMEM) through time (between 0 and 4 days), (D) Mn release of the λ-COS NP in % in different media, (E) T_1 and T_2

measurements of the λ-COS NP in different media. Values were calculated as the mean of three measurements and SD.

Next, experiments were performed to assess Mn release in different media and assess its stability within the NP matrix (**Figure 5D**). For this, the λ-COS NP were ultracentrifuged using a cut-off of 3 kDa and Mn was dosed in the filtrate by ICP-MS. In mQ H_2O, Mn release did not exceed 6% even at 3 h, confirming they remain complexed in this medium. The experiment was also conducted in mouse plasma and, interestingly, a partial release of approximately 20% was observed that remained stable over time. This metal release from the NP in serum should modify its relaxometric characteristics and globally affect the r_1 value of the solution.[64,65] Indeed, it has been shown that free Mn^{2+} ,and its binding to protein carriers in the serum, greatly reduce the tumbling rates, leading to an increase of r_1. Relaxometric values were measured over time in mouse serum and compared to those obtained in mQ H_2O at the same concentration of 0.1 $mg \cdot mL^{-1}$ in Fe + Mn (**Figure 5E**). As expected, due to the initial release of Mn^{2+}, T_1 was immediately observed to be clearly lower in the mouse serum compared to mQ H_2O (34 ms against 160 ms, respectively). It then increased slightly until reaching a plateau of 58 ms at 1 h that is consistent with a re-equilibrium of the system. On the other hand, Mn^{2+} uncoupling from the NP and binding to protein carriers is not supposed to strongly affect T_2 shortening.[65] Indeed, despite T_2 being initially lower than in mQ water, probably owing to protein corona effects and stabilisation of the suspension, it rapidly restored to a similar value of around 40 ms.

3.6 Innocuous profile of λ-COS NP

Injection of λ-CAR is known to induce acute inflammation *in vivo*, promoting the recruitment of immune cells and expression of pro-inflammatory cytokines, which significantly limits its biomedical applications.[66,67] Multiple studies have demonstrated that λ-CAR activates

macrophage responses via pattern recognition receptors, resulting in elevated levels of several cytokines, including tumour necrosis factor alpha (TNF-α), interleukin (IL) 6, IL-8, or IL-1β.[66,68,69] Depolymerisation of λ-CAR to a very low molecular weight (< 10 KDa), however, can reduce or suppress this pro-inflammatory activity.[27] As a pilot experiment to determine whether λ-COS NP display pro-inflammatory behaviour, their effect on the secretion of TNF-α and IL-6 – two key inflammatory markers- was tested in murine RAW 264.7 macrophages and compared to that of λ-CAR and free λ-COS. Before measuring cytokine levels, the impact of each candidate on RAW 264.7 cell viability was assessed over a concentration range of 0-200 $\mu g \cdot mL^{-1}$ using an MTT assay to rule out cytotoxicity and ensure that any changes in cytokine expression were not due to reduced cell populations. The results confirmed that all tested compounds show generally good cell viability across different concentrations (**Figure 6A),** except for λ-COS and λ-COS NP at the highest dose tested (200 $\mu g \cdot mL^{-1}$), where a slight, none-statistically significant effect were, observed**.**

As expected, native λ-CAR treatment at 100 $\mu g \cdot mL^{-1}$ triggered an inflammatory response, evidenced by a marked increase in TNF-α and especially IL-6 production (**Figure 6B** and **6C**). In contrast, cells exposed to λ-COS and λ-COS NP maintained TNF-α and IL-6 levels close to untreated control cells. Overall, these findings provide initial evidence that the depolymerised derivative λ-COS, whether in free solution or as NP coating, does not elicit acute pro-inflammatory effects.

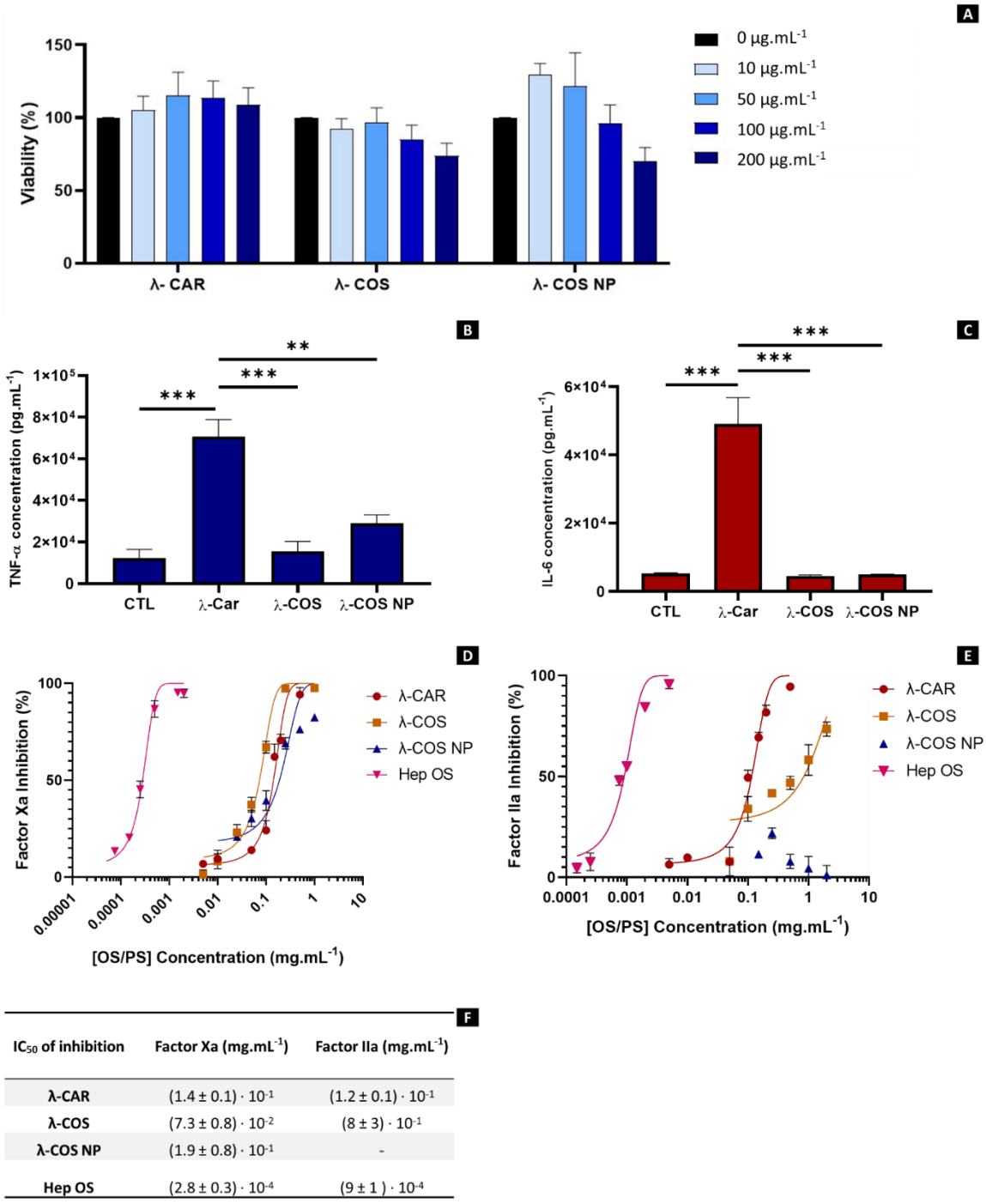

F

IC_{50} of inhibition	Factor Xa ($mg.mL^{-1}$)	Factor IIa ($mg.mL^{-1}$)
λ-CAR	$(1.4 \pm 0.1) \cdot 10^{-1}$	$(1.2 \pm 0.1) \cdot 10^{-1}$
λ-COS	$(7.3 \pm 0.8) \cdot 10^{-2}$	$(8 \pm 3) \cdot 10^{-1}$
λ-COS NP	$(1.9 \pm 0.8) \cdot 10^{-1}$	-
Hep OS	$(2.8 \pm 0.3) \cdot 10^{-4}$	$(9 \pm 1) \cdot 10^{-4}$

Figure 6. (A) Viability of RAW 264.7 macrophages measured by MTT after 24 h incubation with drugs, (B) TNF-α concentration and (C) IL-6 concentration in RAW 264.7 cell media 24 h after incubation with drugs (concentration of 100 $\mu g \cdot mL^{-1}$ in sugar). Values represent mean ± SEM (n = 3), and p-values were calculated using one-way ANOVA with Tukey's multiple

comparison test. Anti-coagulant activity: (C) IC_{50} inhibition of Xa factor and (D) IIa factor (AT III = 0.625 µg.µL-1 and factor Xa or IIa = 11.25 nKat.mL^{-1}), (E) Sum-up of the different IC_{50} activities assessed per drug. Values represent the mean ± SD of triplicate and were fitted through the "absolute IC_{50}" model after normalisation to obtain the IC_{50}.

Another bioactivity of λ-CAR that can limit its applications is its moderate anticoagulant effect.[26] These effects have mainly been ascribed to either AT-III mediated inhibition of factors Xa and thrombin IIa, or to interaction with the heparin cofactor II involved in the coagulation cascade.[70] It has been proposed that λ-CAR follows a mechanism similar to heparin for the inhibition of Xa and IIa, which is effective through the activation of the endogenous modulator anti-thrombin III (AT-III).[71] This mechanism involves the binding of a specific sequence among the polysaccharide to AT-III, leading to a conformational change-based activation that enhances its affinity for the ligand Xa and IIa. For factor IIa inhibition, a minimum chain length is required to directly provide an additional steric hindrance effect on this factor. Inhibition of IIa and Xa factors in the presence of AT-III was assessed for λ-CAR, λ-COS, λ-COS NP, and oligosaccharide of heparin (Hep OS) as an anticoagulant standard (**Figure 6D** and **6E**). IC_{50} were calculated from this data and it appears that λ-CAR inhibited to a significantly lesser degree than the Hep OS for both factors (**Figure 6F**), 0.14 mg·mL^{-1} for Xa and 0.12 mg·mL^{-1} for IIa, against $3 \cdot 10^{-4}$ mg·mL^{-1} and $9 \cdot 10^{-4}$ mg·mL^{-1} respectively. However, it seems that the depolymerisation eased the inhibition of the factor Xa for the λ-COS. Indeed, the IC_{50} observed is $7.3 \cdot 10^{-2}$ mg·mL^{-1}, which is lower than that of the native form. However, the IC_{50} for λ-COS NP was similar to that of the native form (0.19 mg·mL^{-1}), which might be due to steric hindrance preventing the specific sequence from binding to AT-III. For the inhibition of factor IIa, the reduction in chain length had a noticeable effect; the IC_{50} for λ-COS was eight times higher than that of the native

form, with an IC_{50} of 0.8 mg·mL^{-1}. This result is consistent with the molecular weight of λ-COS, which was assessed at a M_n of 3.8 kDa, and was lower than that required to activate the binding of IIa. Concerning λ-COS NP, the inhibition of factor IIa did not exceed 25%, regardless of the concentration of OS, indicating that steric hindrance due to the structural arrangement of the oligosaccharides into NP reinforces the difficulty of binding and form between ATIII, IIa and OS.

Finally, cellular experiments were conducted to explore the potential toxicity of λ-COS NP on epithelial cells prior to *in vivo* experiments. For this, MTT cell viability (**Figure 7A**) and NP cellular uptake assays (**Figure 7B**) were performed in human embryonic kidney cells (HEK293) at various doses in the 0-200 µg·mL^{-1} range and using two incubation times. HEK293 was selected as a convenient standard cell line, widely used in pharmacological assays, including preliminary evaluations of NP cytotoxicity.[72,73] Only λ-COS showed decreased metabolic activity after 24 h at 100 and 200 µg·mL^{-1} concentrations which disappeared after 48 h, while no effect was observed for λ-COS NP at any incubation time. Observations of a decrease in metabolic activity in the early stages of incubation have been previously observed for free polysaccharides and OS, which can reach sublytic concentrations in HEK293 cells, initially affecting their viability, but not causing cell lysis over prolonged time.[74] In any case, this event was not observed for λ-COS NP, providing preliminary indications of the safety of this NP candidate. In addition, after a 24 h incubation with NP, HEK293 cells were fixed and stained with Prussian Blue after a 24 h incubation to reveal the presence of iron. As shown in **Figure 7B,** no internalisation of λ-COS NP was observed.

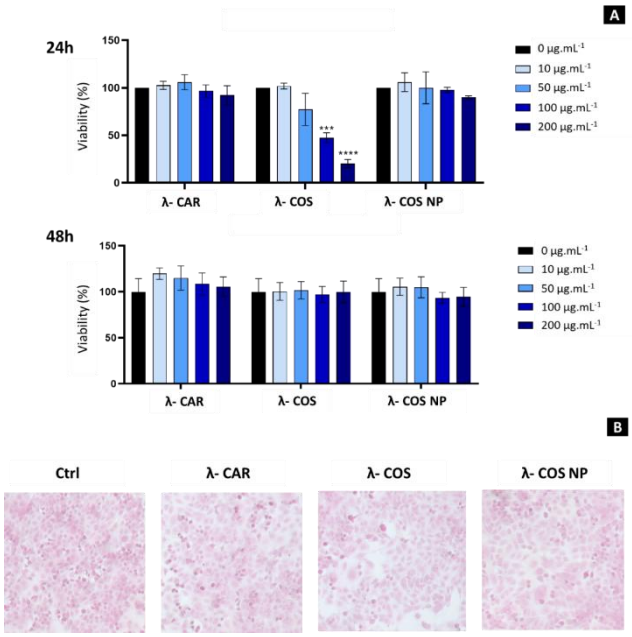

Figure 7. In cellular experiments: (A) Viability of HEK 293 measured by MTT after 24 h and 48 h incubation, (B) NP uptake visualised by Prussian blue staining in HEK293 cells after 24 h incubation ([Fe] = 10 µg·ml^{-1}). Values represent mean ± SEM with N = 3 and n = 3, p values were calculated by one-way ANOVA with Tukey's multiple comparison test.

3.7 MRI (1 Tesla)-based biodistribution studies in mice and imaging applications relating to Mn^{2+} coupling properties.

In vivo MRI studies at 1 Tesla were carried out in healthy mice (n=9, ***Table S12)*** to assess the contrast performance of the λ-COS NP and their *in vivo* behaviour, including vascular lifetime, biodistribution, and clearance from the body. In all cases, λ-COS NP were intravenously (*i.v.*) administered at a dose ranging from 1 to 3 mg·mL^{-1} of (Fe + Mn), and the time course of the signals was recorded for up to 4 h (n=6) or 24 h (n=3). As shown in the T_1-weighted MRI images in ***Figure 8 and Figure S13***, several organs were brightened immediately after the *i.v.* injection of the NP – notably the heart, liver, and kidneys – thereby confirming the positive contrast capability of λ-COS NP. T_2-weighted gradient echo (FLASH) and T1-weighted spin echo

(MSME) sequences were also used, which led to similar results, although contrast enhancements were less pronounced (**Figure S14** and **S15**).

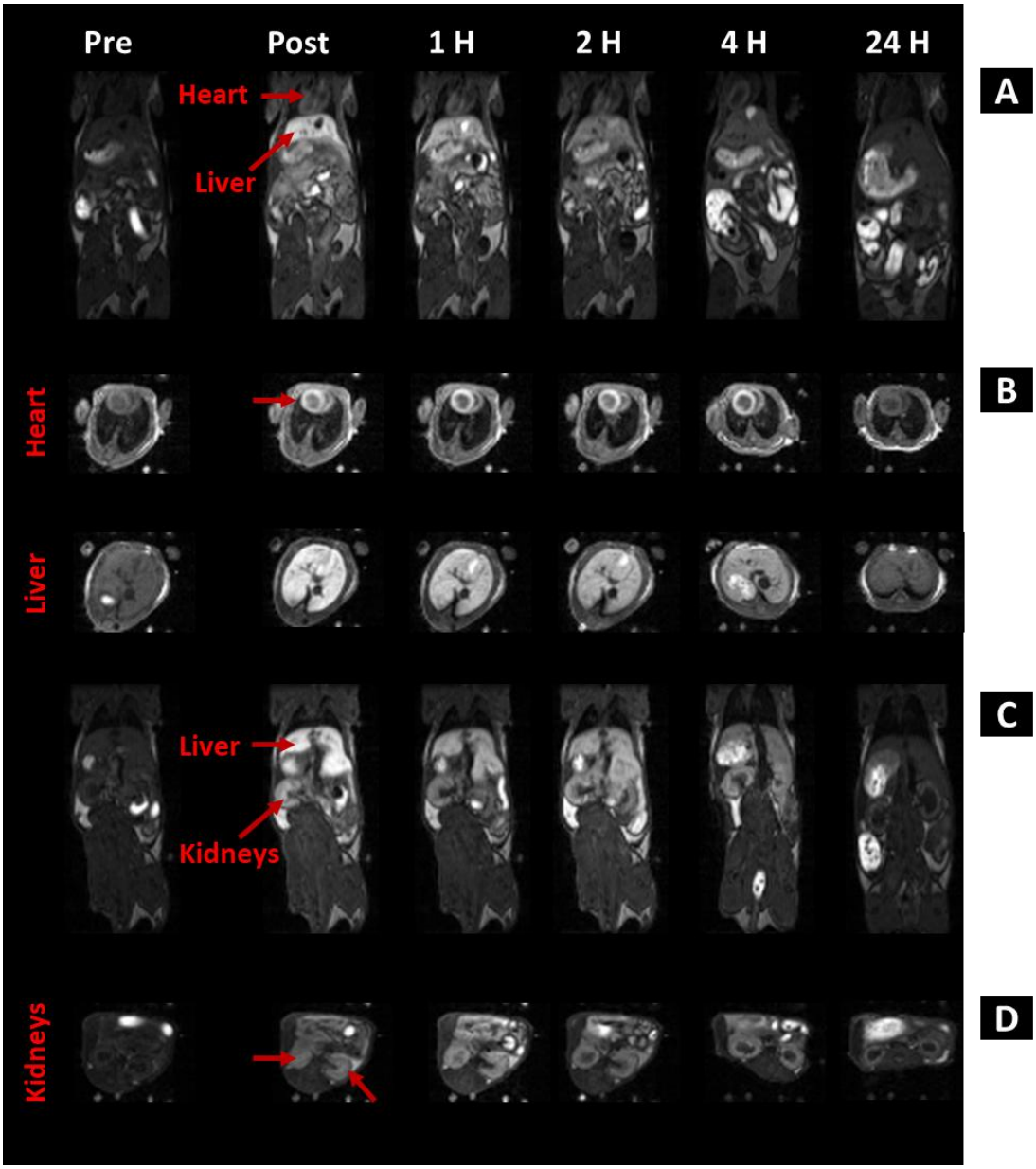

Figure 8. Biodistribution study in MRI at low field (1T) with a T_1-weighted gradient echo sequence of one representative case. Coronal views of upper abdominal region (A) and axial views of the heart and liver (B), additional coronal views of lower abdominal region (C), and

axial views of the kidneys (D). I.v. administration of 100 µL λ-COS NP solution at [Fe + Mn] = 3 $mg \cdot mL^{-1}$.

The intense signals found in the heart with the T_1-weighted sequences mainly accentuate the peripheral myocardium (**Figure 8A, 8B, and S13**), which is strongly indicative of a partial release of Mn^{2+} from the λ-COS NP once entering the blood circulation, consistent with previous *in vitro* experiments. Indeed, a peculiar application in the manganese-enhanced MRI (MEMRI) field relies on the avid uptake of Mn^{2+} ions by the voltage-gated calcium channels of the viable cardiomyocytes, where they can remain for hours.[75] This direct intracellular contrast, paired with the preferential uptake compared to stunned cells, has led to an increasing interest in the characterisation and diagnosis of cardiac pathologies, offering an interesting alternative to gadolinium-based organic chelate contrast agents (GBCA), which allow only the assessment of the extracellular space.[76,77] Despite Mn(II) being an essential endogenous trace element for numerous biological functions and being rapidly cleared from the circulation by hepatocytes, an important issue for this kind of application remains in mitigating the toxicity from Mn overexposure, such as parkinsonism-like symptoms and cardiotoxicity.[78] For this, according to various articles [79], the total Mn dose injected should first be limited to a concentration below those reported to cause detectable adverse effects that is estimated between 200 and 500 $\mu M \cdot kg^{-1}$. The doses used in this study were approximately in the 25 - 95 $\mu M \cdot kg^{-1}$ range (**Table S12**) and still, a significant contrast enhancement in various organs was achieved. Second, one common approach used to reduce the risks of Mn toxicity, while maintaining a suitably low level of free Mn^{2+} in circulation, is to complex the metallic ion within a ligand that allows controlled partial uncoupling in the plasma, facilitating its circulation as a protein-bound complex. In this way, a more persistent releasable Mn^{2+} source and buffered lower concentration for intracellular

contrast can be achieved, with a predominant prolonged hepatobiliary clearance.[65,78,80] This approach even led to a marketed product based on manganese dipyridoxyl diphosphate (Mn-DPDP, Telascan®), initially intended for use as contrast agents for liver and gastrointestinal imaging. It has since been superseded by the greater efficiency of GBCA and a lack of demand, but it is still applied in pre-clinical studies and new clinical trials, especially for heart diagnosis-based MEMRI.[65,77]

Here, a comparable behaviour occurred for λ-COS NP. Accordingly, in the heart, signals were maintained for up to 4 h, as shown in **Figures 8A** and **8B**, due to the partial release of Mn^{2+} (limited to 20% in plasma as measured *in vitro* previously) and binding to blood proteins (as indicated *in vitro* previously by the increase of r_1 in serum), before uptake by the cardiomyocytes. Similar to Mn-DPDP and related to its initial purpose, a significant brightening in the liver also appeared immediately after *i.v.* administration (**Figure 8A-C** and **S13**), owing to Mn^{2+} uptake by hepatocytes, and lasted up to 4 h with a progressive decrease in the contrast enhancement ratio. In tandem, an intense signal was gradually detected in the gallbladder (**Figure 8A, 8B** and **S13**) and biliary tree, peaking at 2 h before vanishing entirely at 24 h. As a control and for the comparison of NP contrast performance, Multihance® (gadobenic acid), a liver-specific contrast agent was used (**Figure S16**). As seen on the images, the MRI signal intensities were higher for the λ-COS NP than for the GBCA and lasted longer, even with a lower Mn dose administered (~24 $\mu M \cdot kg^{-1}$) compared to the Gd dose (~116 $\mu M \cdot kg^{-1}$). This observation is interesting, as GBCA are often preferred to Mn-based contrast agents due to their typical higher contrast efficiency achieved with a smaller dose of administered metallic ions, even if they do not offer the advantage of delayed contrast. Two hypotheses were proposed to explain this encouraging result: the partial excretion of Gadobenic acid through the urine, leading

to a lower effective dose transiting in the liver; and/or an additional "contrast contribution" to the released Mn^{2+}- originating positive contrast. This last might come, for instance, from the metabolized λ-COS NP encapsulating the extremely small ferrite cores, which can also produce a positive contrast. Finally, signals in the kidneys were also examined during the study (**Figures 8C**, **8D,** and **S13**). Contrast enhancements were also visible until 4 h with a residual at 24 h, especially brightening the vascularised cortex/medulla region, whereas no detectable signal was found in the bladder throughout the time course of the experiments. Again, these results align well with previous MRI-based biodistribution studies of Mn-DPDP[80], which revealed signals in this organ in the first hours after *i.v.* administration, attributed to free or complexed Mn^{2+} circulating in the blood, and also showed moderate accumulation (< 20%) of the metabolised probe after 24 h.

3.8 MRI (7 Tesla)-based biodistribution studies in mice for studying the influence of the λ-COS coating on the NP in vivo behaviour.

The focus was then directed towards the λ-COS NP framework encapsulating the ferrite cores, to study the bio-interactions and pharmacokinetic properties conferred to NP by this new carbohydrate-based coating. At low field, ferrite cores exhibit T_1-contrast ability due to their extremely small size; however, in our situation, such a contrast could therefore be confused with that of the free released Mn^{2+}, making it difficult to discern the biodistribution of the intact λ-COS NP. In view of this, it was advisable to rely on the strong T_2 contrast properties found for the λ-COS NP at high field (r_2/r_1 ratio of 22.9 at 7 Tesla), which mainly come from the ferrite cores, even if free Mn^{2+} should also exhibit minor T_2-relaxation shortening properties. *In vivo* experiments in mice with *i.v.* administration of λ-COS NP at three different doses ([Fe + Mn] at 0.8, 1.3 and 1.5 mg mL^{-1}, n=2 for each, n=6 total) were therefore repeated using a 7 Tesla

scanner, and images were recorded by a MSME (Multi slice Spin echo) sequence to build the T2 relaxometric maps before injection, at post-injection (0.5 h – 2 h), and at 24 h. See **Table S12** for details about doses and times of acquisitions. Representative T2 maps obtained in mice are shown in **Figure 9A and S17**, and the mean T_2-values of selected ROIs in different organs were calculated for each dose administered, pooling together all the pre-contrast and post-contrast points of the two mice (**Figure 9B** and **S18**). Regarding the liver, a strong decrease in the T2 values was observed post injection (0.5-2 h) in all cases, which only partially recovered after 24 h. It has been previously shown in the 1-Tesla experiments that released Mn^{2+} were already eliminated after 24 h in the intestinal tree and should not, therefore, have been contributing to the MRI signals anymore. It is for this reason that this T2-reduction that was still seen at that time is particularly interesting, as it strongly indicates that a part of intact λ-COS NP was taken up by hepatic macrophages. With respect to the change in the T_2-values in the kidneys, a significant decrease was also observed post-injection (0.5-2 h). This is more likely due to circulating NP, detected because of the high vascularisation of the cortex and medulla[81], rather than renal clearance of λ-COS NP through the urinary system. Indeed, the HD of NP was larger than the renal filtration threshold (estimated at approximately 8 nm), and no T_2 shortening was observed in the bladder, making this possibility improbable. Interestingly, T_2-shortening in the cortex and medulla was detected, even 2 h after the lowest dose was administered (**Figure S18**), which suggests that λ-COS NP have blood pool properties that are potentially advantageous for targeting pathological tissue. However, this hypothesis should be taken with caution because released Mn^{2+} could also make a small contribution to the signal and be confused with that of the intact λ-COS NP. This could explain the T2 values found in the kidneys at 24 h, which had almost recovered to their basal values, but with a small reminiscent signal that may come from

metabolized forms of Mn^{2+}, consistent with the previous 1 Tesla MRI experiments. Finally, to round out the picture, it can be noticed that a small decrease in T_2 was detected in the spleen, another organ commonly involved in NP elimination.[82] It can be reasonably attributed to only λ-COS NP, as released Mn^{2+} is not supposed to accumulate in this organ[80], and, besides, it was not detected in 1 Tesla MRI.

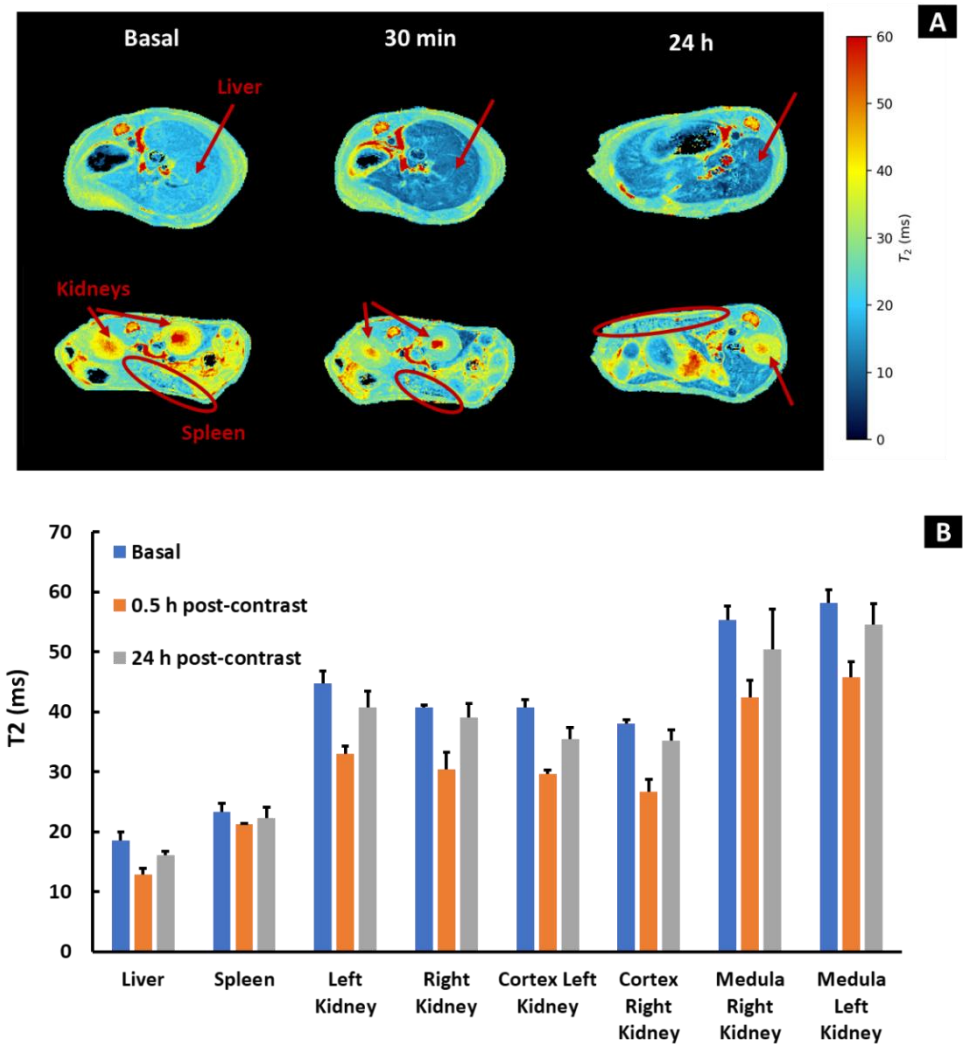

Figure 9. Biodistribution study in MRI at high field (7T) with (A) T_2-Relaxometric maps in cross sections obtained from a MSME sequence (TE varied in 20 steps from 8 to 160 ms, TR=4000 ms, FA 90°). (B) T_2-value quantification in selected ROI of different organs, pooling

together the contrast points of two mice (i.v. administration of 70 µL λ-COS NP solution: [Fe + Mn] = 1.5 mg mL^{-1}).

3.9 Ex-vivo analyses

To further explore the biodistribution of λ-COS NP and their metabolites (especially released Mn^{2+}), *ex vivo* analyses were conducted. For this, the main organs of the RES system were collected and perfused at 3 h (n= 2) and 24 h (n= 1) following i.v. administration of NP (see ***Table* S12** for doses). A histological analysis of tissue sections, stained with haematoxylin-eosin, was first performed as a preliminary indication of the potential toxicity induced by λ-COS NP or free Mn^{2+}. No obvious pathological changes in the main organs were noticed in the images, either at 3 h or at 24 h (**Figure 10A** and **S19**, respectively). Next, Prussian blue staining was performed to reveal the *in vivo* iron-containing λ-COS NP distribution. At 3 h and 24 h, numerous distinguishable blue dots were detected in the liver tissue corresponding to the Fe contained in the ferrite cores and colocalizing with the Kupffer cells (**Figure 10A** and **S19**). This confirms the previous results obtained with the MSME-based 7 Tesla MRI, which showed that a part of the λ-COS NP was eliminated in the hepatic macrophages. Iron-containing cores were also detected in the lungs at 3 h, and to a minor extent at 24 h, indicating that NP lodged temporarily in small lung capillaries – a phenomenon frequently observed for NP with a HD up to 50 nm. Unfortunately, it was impossible to visualise any accumulation of NP in the spleen, as it already contained many endogenous iron forms that had been detected on the control image. In the other organs examined, no blue dots were clearly noticeable in either the intestines at 3 h, which may indicate that the "intact" NP did not undergo hepatobiliary clearance such as Mn^{2+}, or in the heart, confirming that only released Mn^{2+} was taken up by myocytes. Regarding the kidneys, the absence of blue dots at 3 h and 24 h confirmed that 7 Tesla-MRI signals detected

were more likely due to circulating NP (flushed during the *ex vivo*-perfusion step) than to accumulated NP in the tissue.

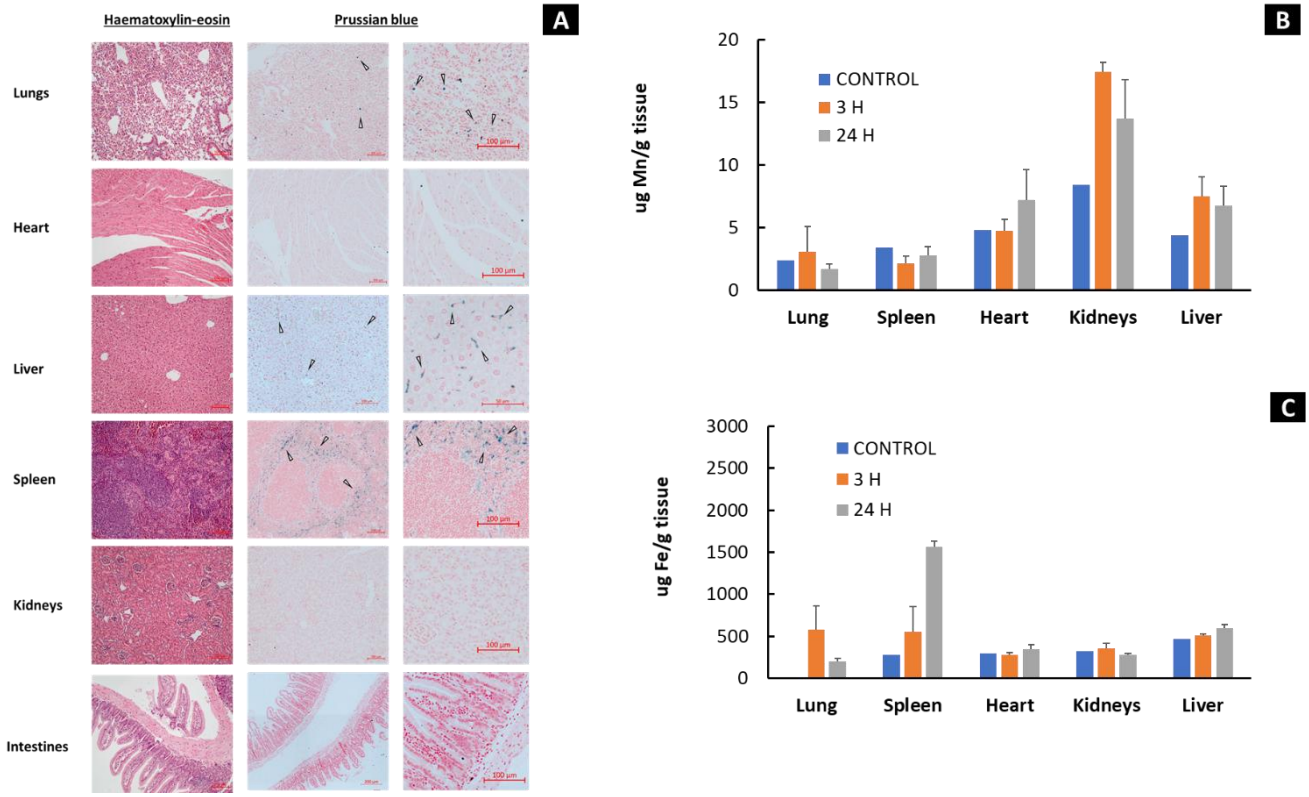

Figure 10. (A) Histopathology in main organs 3 h after injection, stained by haematoxylin and eosin and Prussian blue, observed by optical microscopy at 20x and 40x. Injected volume: 70 µL, [Fe + Mn] = 1.5 mg·mL^{-1} (n=2). Black and white arrows point out the blue stains on Prussian blue images. (B) Mn and (C) Fe contents in the organs, measured by ICP-MS and expressed in mass (µg) of Mn per g of dry tissue. The data are mean ± SEM of n=2 mice at 3 h and n=4 mice at 24 h.

Mn and Fe were quantified in the organs by ICP-MS to provide information about the biodistributions of the Mn released and λ-COS NP' associated ferrite cores, respectively. Concerning Mn dosage (**Figure 10B**), average Mn concentrations (µg/g of dry tissue) were

higher in the kidneys and liver 3 h after the injection (n=2) compared than at the physiological basal level. This result is in good agreement with the pharmacokinetic properties observed in the 1 Tesla MRI-based biodistribution studies, where released Mn^{2+} from the NP was still circulating at that time, combined with avid uptake by hepatocytes. A decrease in the Mn level, although still above the basal level, was then obtained at 24 h in both organs (n=4). Again, this fits well with the 1 Tesla-MRI signals found at that time in the kidneys. It indicates the weak accumulation of Mn in this organ, while the higher concentration in the liver may come from either remaining Mn^{2+} ions, or from the λ-COS NP ferrite cores found in hepatic macrophages that also contain a small amount of Mn doping. Surprisingly, no significant enhancement in Mn concentration was found at 3 h in the heart to align with their uptake by the voltage-gated calcium channels of the cardiomyocytes observed on 1 Tesla MRI. Concerning iron dosage (**Figure 10C**), higher average Fe concentrations compared to basal values were found in the spleen and liver at both 3 h (n=2) and 24 h (n=4). It should be noted here that the concentration is expressed in µg/g of dry tissue and should be balanced in accordance with the organ weights (much higher in the case of the liver). This is consistent with the presence of λ-COS NP encapsulating ferrite cores in the Kupffer cells, as well as their accumulation in the spleen, which was previously observed during 7 Tesla MRI-based biodistribution experiments and confirmed by histology. In Kidneys, no additional iron level compared to basal was noticed at either time, confirming that 7 Tesla-MRI signals detected at 3 h, in particular, were more likely due to circulating NP (flushed at the *ex vivo*-perfusion step) than to NP accumulated in tissue. Finally, a transient excess of iron was measured in the lungs 3 h following the NP injection, before a decrease was observed towards the baseline value by 24 h that was consistent with the histological observations.

To complete the *ex vivo* analysis, ICP-MS was also carried out on urine samples collected during the different experiments and did not reveal any significant change in Mn or Fe concentration. This provides an additional indication regarding the absence of renal clearance for this probe and its associated metabolites (data not shown). Measurements were also done on the intestine and collected faeces, but results should be interpreted with caution as mice were not fasted in this study. While Mn concentration (μg/g of dry tissue) remained roughly similar in the intestine (**Figure S20**), some faecal samples exhibited unusually high levels of Mn, in accordance with the clearance of released Mn^{2+} through the intestinal tract (data not shown). Uncovering information from the Fe dosage was more challenging. This was due to the already high basal level in faeces, even if it appears that Fe levels were surprisingly lower (data not shown), while concentration in the intestine displayed an increase in concentration (**Figure S20**). It could be suggested that degradation of ferrite cores confined in hepatic macrophages could initiate a progressive release of metabolised iron retained in the intestine.

4. Conclusions

In this study, depolymerised derivatives of λ-CAR were evaluated as potential NP scaffolds for exploring novel chemistries, specific functionalities, and *in vivo* bio-interactions. Initial results in cell-based models and *in vitro* assays indicated that λ-COS and λ-COS-NP exhibited substantially higher biocompatibility than native λ-CAR, particularly demonstrating reduced pro-inflammatory activity. The use of λ-COS also improved solubility compared to λ-CAR and decreased viscosity, thereby simplifying NP synthesis. Under microwave-assisted conditions, the resulting nanostructure was a λ-COS-based hybrid NP, in which the λ-COS scaffold served both as a coating to encapsulate ferrite cores and as a macromolecular chelator for Mn^{2+} ions. Advanced electronic microscopy and spectroscopy techniques revealed that the cores formed

crystalline structures in a mixed spinel arrangement. In parallel, substitution with Zn^{2+} verified the specific stabilization of Mn^{2+} ions by chemical groups within the organic matrix rather than by non-specific adsorption at the surface of the NP. Subsequent magnetometry studies confirmed the presence of both ferrite cores and a population of complexed Mn ions in the NP. Relaxometric measurements further showed that the NP exhibited different contrast properties in MRI, depending on the applied magnetic field and the contributions from free Mn^{2+}, complexed Mn^{2+} and ferrite cores. Finally, *in vitro* stability tests demonstrated that the complete NP remained stable in aqueous media, while approximately 20% of the Mn^{2+} payload was released in serum.

In vivo MRI studies in mice using a 1 Tesla scanner indicated that the λ-COS NP, in their "Mn-releasable complex" configuration, are suitable for a typical application of Mn^{2+} -based intracellular contrast in MEMRI, specifically for imaging the myocardium and the hepatobiliary system. The observed biodistribution and clearance profiles were similar to those typically reported for Mn-DPDP, an FDA-approved ligand that controls the release of Mn^{2+} *in vivo*, thereby reducing potential toxicity concerns. Further MRI examinations at 7 Tesla along with *ex-vivo* studies suggest that the λ-COS NP, in their "ferrite core coating" configuration, exhibit a good vascular lifetime relative to other polysaccharide-based NP and undergo at least partially, clearance by hepatic macrophages.

Future investigations are necessary to more clearly distinguish these two functionalities. For instance, synthetizing λ-COS-based NP without ferrite cores will allow a deeper exploration of the metallation chemistry, particularly as macromolecular Mn^{2+} chelates. Such a study could confirm the gradual release of Mn^{2+} properties in serum to avoid overexposure, clarify the role of sub-metabolites following i.v. administration (including the possibility that retained Mn^{2+} in λ-

COS NP may lead to distinct biodistribution in pathological tissue), and assess the overall contrast performance as an alternative to GBCA. Additionally, different synthetic routes could be employed to prepare "single" λ-COS coated metallic NP cores. This approach would aid in clarifying how the oligosaccharide coating influences pharmacokinetic properties, biodistribution, and clearance of metallic NP, while also enabling further evaluation of potential biofunctional roles of λ-COS in NP formulations, such as targeted delivery or therapeutic activity.

Nevertheless, the λ-COS NP exhibiting this "dual feature" may offer potential advantages for specific bioapplications. For example, the probe could function as a theragnostic agent responsive to the tumour microenvironment, releasing Mn^{2+} ions more efficiently under acidic conditions. The resulting strong contrast enhancement may confirm accumulation at the tumour site, while additional bioactivities could arise from the λ-COS coating, the ferrite core, or the released Mn^{2+}.

ASSOCIATED CONTENT

Supporting Information

Figure S1: SEC-HPLC spectra of λ-COS, Figure S2: FT-IR and UV-visible spectra of metals-λ-COS coordination complex, Figure S3: Mn released assessment, Figure S4: TEM and HRTEM images, Figure S5: HRTEM images associated with EDS in maps, Figure S6: HRTEM images associated with EDS in line, Figure S7: Diffraction pattern and d-spacing, Table S8: Estimation of number of COS Fe and Mn per NP, Figure S9: XPS characterization, Figure S10: Magnetic moment at different temperatures, Figure S11: Phantoms at 1T and 7T, Table S12: Table listing

the in vivo experiments, Figure S13: MRI (1T) images (T1-GE sequence), Figure S14: MRI (1T) images (T2-GE sequence), Figure S15: MRI (1T) images (MSME sequence), Figure S16: Comparison of contrast performance with Multihance® , Figure S17: MRI (7T) images, Figure S18: T2-value quantification in selected ROI of different organs, Figure S19: Histopathology, 24 h after the injection, Figure S20: Mn and Fe content in intestine measured by ICP-MS.

Author Contributions

The manuscript was written through contributions of all authors. All authors have given approval to the final version of the manuscript.

ACKNOWLEDGMENT

This work was financially supported by La Ligue contre le Cancer (comité 16 de Charente and 17 de Charente Maritimes), the French National Research Agency (ANR-22-CE18-0028, Project NANOLIGO), and the Région Nouvelle-Aquitaine (Nanovect and Oligovect projects).

JRC is funded by MCIN/AEI (PID2021-123238OB-I00), Basque Government under the Elkartek 2024 Program (bmG24) and R&D Projects in Health (Grant no. 2022333041). SCR was funded by MCIN/AEI (CNS2023-143944, RYC2020-030241-I, PID2022-142842OB-I00) and the Ikerbasque and Ramon Areces Foundation (CIVP21S13151). The *in vivo* work was carried out at the ReDIB ICTS infrastructure at CIC biomaGUNE and BioImaC, Ministry of Science, Innovation and Universities (MCIU)

REFERENCES

(1) *Polysaccharide-based nanoparticles for theranostic nanomedicine - ScienceDirect*. https://www.sciencedirect.com/science/article/abs/pii/S0169409X15002793 (accessed 2024-04-12).

(2) Venkatesan, J.; Anil, S.; Kim, S.-K.; Shim, M. S. Seaweed Polysaccharide-Based Nanoparticles: Preparation and Applications for Drug Delivery. *Polymers* **2016**, *8* (2), E30. https://doi.org/10.3390/polym8020030.

(3) Plucinski, A.; Lyu, Z.; J. Schmidt, B. V. K. Polysaccharide Nanoparticles: From Fabrication to Applications. *J. Mater. Chem. B* **2021**, *9* (35), 7030–7062. https://doi.org/10.1039/D1TB00628B.

(4) Rodriguez-Torres, M. del P.; Acosta-Torres, L. S.; Diaz-Torres, L. A. Heparin-Based Nanoparticles: An Overview of Their Applications. *J. Nanomater.* **2018**, *2018*, e9780489. https://doi.org/10.1155/2018/9780489.

(5) Naha, P. C.; Liu, Y.; Hwang, G.; Huang, Y.; Gubara, S.; Jonnakuti, V.; Simon-Soro, A.; Kim, D.; Gao, L.; Koo, H.; Cormode, D. P. Dextran-Coated Iron Oxide Nanoparticles as Biomimetic Catalysts for Localized and pH-Activated Biofilm Disruption. *ACS Nano* **2019**, *13* (5), 4960–4971. https://doi.org/10.1021/acsnano.8b08702.

(6) Unsoy, G.; Yalcin, S.; Khodadust, R.; Gunduz, G.; Gunduz, U. Synthesis Optimization and Characterization of Chitosan-Coated Iron Oxide Nanoparticles Produced for Biomedical Applications. *J. Nanoparticle Res.* **2012**, *14* (11), 964. https://doi.org/10.1007/s11051-012-0964-8.

(7) Campo, V. L.; Kawano, D. F.; Silva, D. B. da; Carvalho, I. Carrageenans: Biological Properties, Chemical Modifications and Structural Analysis – A Review. *Carbohydr. Polym.* **2009**, *77* (2), 167–180. https://doi.org/10.1016/j.carbpol.2009.01.020.

(8) Geonzon, L. C.; Descallar, F. B. A.; Du, L.; Bacabac, R. G.; Matsukawa, S. Gelation Mechanism and Network Structure in Gels of Carrageenans and Their Mixtures Viewed at Different Length Scales – A Review. *Food Hydrocoll.* **2020**, *108*, 106039. https://doi.org/10.1016/j.foodhyd.2020.106039.

(9) Shafie, M. H.; Kamal, M. L.; Zulkiflee, F. F.; Hasan, S.; Uyup, N. H.; Abdullah, S.; Mohamed Hussin, N. A.; Tan, Y. C.; Zafarina, Z. Application of Carrageenan Extract from Red Seaweed (Rhodophyta) in Cosmetic Products: A Review. *J. Indian Chem. Soc.* **2022**, *99* (9), 100613. https://doi.org/10.1016/j.jics.2022.100613.

(10) Sharma, G.; Khosla, A.; Kumar, A.; Kaushal, N.; Sharma, S.; Naushad, M.; Vo, D.-V. N.; Iqbal, J.; Stadler, F. J. A Comprehensive Review on the Removal of Noxious Pollutants Using Carrageenan Based Advanced Adsorbents. *Chemosphere* **2022**, *289*, 133100. https://doi.org/10.1016/j.chemosphere.2021.133100.

(11) Liu, H.; Håkansson, K. Electron Capture Dissociation of Divalent Metal-Adducted Sulfated Oligosaccharides. *Int. J. Mass Spectrom.* **2011**, *305* (2), 170–177. https://doi.org/10.1016/j.ijms.2010.10.030.

(12) Rotureau, E.; van Leeuwen, H. P. Kinetics of Metal Ion Binding by Polysaccharide Colloids. *J. Phys. Chem. A* **2008**, *112* (31), 7177–7184. https://doi.org/10.1021/jp800472g.

(13) García Tasende, M.; Manriquez-Hernandez, J. Carrageenan Properties and Applications: A Review. In *Carrageenans: Sources and Extraction Methods, Molecular Structure, Bioactive Properties and Health Effects*; 2016; pp 17–50.

(14) Liu, Z.; Gao, T.; Yang, Y.; Meng, F.; Zhan, F.; Jiang, Q.; Sun, X. Anti-Cancer Activity of Porphyran and Carrageenan from Red Seaweeds. *Molecules* **2019**, *24* (23), 4286. https://doi.org/10.3390/molecules24234286.

(15) Prasedya, E. S.; Miyake, M.; Kobayashi, D.; Hazama, A. Carrageenan Delays Cell Cycle Progression in Human Cancer Cells in Vitro Demonstrated by FUCCI Imaging. *BMC Complement. Altern. Med.* **2016**, *16*. https://doi.org/10.1186/s12906-016-1199-5.

(16) Jazzara, M.; Ghannam, A.; Soukkarieh, C.; Murad, H. Anti-Proliferative Activity of λ-Carrageenan Through the Induction of Apoptosis in Human Breast Cancer Cells. *Iran. J. Cancer Prev.* **2016**, *9* (4), e3836. https://doi.org/10.17795/ijcp-3836.

(17) *How to manage anticoagulation for cancer-associated thrombosis and atrial fibrillation in cancer - ScienceDirect*. https://www.sciencedirect.com/science/article/pii/S2666572724000117 (accessed 2025-01-27).

(18) Patriota, Y. B. G.; Chaves, L. L.; Gocke, E. H.; Severino, P.; Soares, M. F. R.; Soares-Sobrinho, J. L.; Souto, E. B. Applied Nanotechnologies in Anticoagulant Therapy: From Anticoagulants to Coagulation Test Performance of Drug Delivery Systems. *Appl. Nano* **2021**, *2* (2), 98–117. https://doi.org/10.3390/applnano2020009.

(19) Daniel-da-Silva, A. L.; Trindade, T.; Goodfellow, B. J.; Costa, B. F. O.; Correia, R. N.; Gil, A. M. In Situ Synthesis of Magnetite Nanoparticles in Carrageenan Gels. *Biomacromolecules* **2007**, *8* (8), 2350–2357. https://doi.org/10.1021/bm070096q.

(20) Kim, J.; Lee, K.-Y.; Lee, C.-M. Selenium Nanoparticles Formed by Modulation of Carrageenan Enhance Osteogenic Differentiation of Mesenchymal Stem Cells. *J. Nanosci. Nanotechnol.* **2016**, *16* (3), 2482–2487. https://doi.org/10.1166/jnn.2016.10764.

(21) Abdullah, S.; El Hadad, S.; Aldahlawi, A. The Development of a Novel Oral 5-Fluorouracil in-Situ Gelling Nanosuspension to Potentiate the Anticancer Activity against Colorectal Cancer Cells. *Int. J. Pharm.* **2022**, *613*, 121406. https://doi.org/10.1016/j.ijpharm.2021.121406.

(22) Kurosaki, T.; Kitahara, T.; Kawakami, S.; Nishida, K.; Nakamura, J.; Teshima, M.; Nakagawa, H.; Kodama, Y.; To, H.; Sasaki, H. The Development of a Gene Vector Electrostatically Assembled with a Polysaccharide Capsule. *Biomaterials* **2009**, *30* (26), 4427–4434. https://doi.org/10.1016/j.biomaterials.2009.04.041.

(23) Bulmer, C.; Margaritis, A.; Xenocostas, A. Encapsulation and Controlled Release of Recombinant Human Erythropoietin from Chitosan-Carrageenan Nanoparticles. *Curr. Drug Deliv.* **2012**, *9* (5), 527–537. https://doi.org/10.2174/156720112802650680.

(24) *Gd(DOTA)-grafted submicronic polysaccharide-based particles functionalized with fucoidan as potential MR contrast agent able to target human activated platelets - ScienceDirect*. https://www.sciencedirect.com/science/article/pii/S0144861720306317 (accessed 2024-12-10).

(25) *Radiolabeled Fucoidan as a P-Selectin Targeting Agent for In Vivo Imaging of Platelet-Rich Thrombus and Endothelial Activation | Journal of Nuclear Medicine*. https://jnm.snmjournals.org/content/52/9/1433.long (accessed 2024-12-10).

(26) Groult, H.; Cousin, R.; Chot-Plassot, C.; Maura, M.; Bridiau, N.; Piot, J.-M.; Maugard, T.; Fruitier-Arnaudin, I. λ-Carrageenan Oligosaccharides of Distinct Anti-Heparanase and Anticoagulant Activities Inhibit MDA-MB-231 Breast Cancer Cell Migration. *Mar. Drugs* **2019**, *17* (3), 140. https://doi.org/10.3390/md17030140.

(27) Guo, Z.; Wei, Y.; Zhang, Y.; Xu, Y.; Zheng, L.; Zhu, B.; Yao, Z. Carrageenan Oligosaccharides: A Comprehensive Review of Preparation, Isolation, Purification, Structure, Biological Activities and Applications. *Algal Res.* **2022**, *61*, 102593. https://doi.org/10.1016/j.algal.2021.102593.

(28) Álvarez-Viñas, M.; Souto, S.; Flórez-Fernández, N.; Torres, M. D.; Bandín, I.; Domínguez, H. Antiviral Activity of Carrageenans and Processing Implications. *Mar. Drugs* **2021**, *19* (8), 437. https://doi.org/10.3390/md19080437.

(29) Chen, H.; Yan, X.; Lin, J.; Wang, F.; Xu, W. Depolymerized Products of Lambda-Carrageenan as a Potent Angiogenesis Inhibitor. *J. Agric. Food Chem.* **2007**, *55* (17), 6910–6917. https://doi.org/10.1021/jf070183+.

(30) Chen, X.; Han, W.; Zhao, X.; Tang, W.; Wang, F. Epirubicin-Loaded Marine Carrageenan Oligosaccharide Capped Gold Nanoparticle System for pH-Triggered Anticancer Drug Release. *Sci. Rep.* **2019**, *9* (1), 6754. https://doi.org/10.1038/s41598-019-43106-9.

(31) Youssouf, L.; Bhaw-Luximon, A.; Diotel, N.; Catan, A.; Giraud, P.; Gimié, F.; Koshel, D.; Casale, S.; Bénard, S.; Meneyrol, V.; Lallemand, L.; Meilhac, O.; Lefebvre D'Hellencourt, C.; Jhurry, D.; Couprie, J. Enhanced Effects of Curcumin Encapsulated in Polycaprolactone-Grafted Oligocarrageenan Nanomicelles, a Novel Nanoparticle Drug Delivery System. *Carbohydr. Polym.* **2019**, *217*, 35–45. https://doi.org/10.1016/j.carbpol.2019.04.014.

(32) Wathoni, N.; Meylina, L.; Rusdin, A.; Mohammed, A. F. A.; Tirtamie, D.; Herdiana, Y.; Motoyama, K.; Panatarani, C.; Joni, I. M.; Lesmana, R.; Muchtaridi, M. The Potential Cytotoxic Activity Enhancement of α-Mangostin in Chitosan-Kappa Carrageenan-Loaded Nanoparticle against MCF-7 Cell Line. *Polymers* **2021**, *13* (11), 1681. https://doi.org/10.3390/polym13111681.

(33) Johnson, A.; Kong, F.; Miao, S.; Thomas, S.; Ansar, S.; Kong, Z.-L. In-Vitro Antibacterial and Anti-Inflammatory Effects of Surfactin-Loaded Nanoparticles for Periodontitis Treatment. *Nanomaterials* **2021**, *11* (2), 356. https://doi.org/10.3390/nano11020356.

(34) Li, Z.; Wang, S. X.; Sun, Q.; Zhao, H. L.; Lei, H.; Lan, M. B.; Cheng, Z. X.; Wang, X. L.; Dou, S. X.; (Max) Lu, G. Q. Ultrasmall Manganese Ferrite Nanoparticles as Positive Contrast Agent for Magnetic Resonance Imaging. *Adv. Healthc. Mater.* **2013**, *2* (7), 958–964. https://doi.org/10.1002/adhm.201200340.

(35) Miao, Y.; Xie, Q.; Zhang, H.; Cai, J.; Liu, X.; Jiao, J.; Hu, S.; Ghosal, A.; Yang, Y.; Fan, H. Composition-Tunable Ultrasmall Manganese Ferrite Nanoparticles: Insights into Their *In Vivo* T_1 Contrast Efficacy. *Theranostics* **2019**, *9* (6), 1764–1776. https://doi.org/10.7150/thno.31233.

(36) *Manganese ferrite (MnFe2O4) nanostructures for cancer theranostics - ScienceDirect*. https://www.sciencedirect.com/science/article/pii/S0010854522004040 (accessed 2024-11-21).

(37) Achour, O.; Poupard, N.; Bridiau, N.; Bordenave Juchereau, S.; Sannier, F.; Piot, J.-M.; Fruitier Arnaudin, I.; Maugard, T. Anti-Heparanase Activity of Ultra-Low-Molecular-Weight Heparin Produced by Physicochemical Depolymerization. *Carbohydr. Polym.* **2016**, *135*, 316–323. https://doi.org/10.1016/j.carbpol.2015.08.041.

(38) Poupard, N.; Groult, H.; Bodin, J.; Bridiau, N.; Bordenave-Juchereau, S.; Sannier, F.; Piot, J.-M.; Fruitier-Arnaudin, I.; Maugard, T. Production of Heparin and λ-Carrageenan Anti-Heparanase Derivatives Using a Combination of Physicochemical Depolymerization and Glycol Splitting. *Carbohydr. Polym.* **2017**, *166*, 156–165. https://doi.org/10.1016/j.carbpol.2017.02.040.

(39) Carregal-Romero, S.; Miguel-Coello, A. B.; Martínez-Parra, L.; Martí-Mateo, Y.; Hernansanz-Agustín, P.; Fernández-Afonso, Y.; Plaza-García, S.; Gutiérrez, L.; Muñoz-Hernández, M. del M.; Carrillo-Romero, J.; Piñol-Cancer, M.; Lecante, P.; Blasco-Iturri, Z.; Fadón, L.; Almansa-García, A. C.; Möller, M.; Otaegui, D.; Enríquez, J. A.; Groult, H.; Ruíz-Cabello, J. Ultrasmall Manganese Ferrites for In Vivo Catalase Mimicking Activity and Multimodal Bioimaging. *Small* **2022**, *18* (16), 2106570. https://doi.org/10.1002/smll.202106570.

(40) Cao, Y.; Li, S.; Fang, Y.; Nishinari, K.; Phillips, G. O.; Lerbret, A.; Assifaoui, A. Specific Binding of Trivalent Metal Ions to *λ*-Carrageenan. *Int. J. Biol. Macromol.* **2018**, *109*, 350–356. https://doi.org/10.1016/j.ijbiomac.2017.12.095.

(41) Raman, M.; Devi, V.; Doble, M. Biocompatible ι-Carrageenan-γ-Maghemite Nanocomposite for Biomedical Applications – Synthesis, Characterization and in Vitro

Anticancer Efficacy. *J. Nanobiotechnology* **2015**, *13* (1), 18. https://doi.org/10.1186/s12951-015-0079-3.

(42) Oya, K.; Tsuru, T.; Teramoto, Y.; Nishio, Y. Nanoincorporation of Iron Oxides into Carrageenan Gels and Magnetometric and Morphological Characterizations of the Composite Products. *Polym. J.* **2013**, *45* (8), 824–833. https://doi.org/10.1038/pj.2012.221.

(43) Shu, M.; Yao, X.; Wu, K.; Zhang, K.; Nishinari, K.; Phillips, G. O.; Yao, X.; Jiang, F. Preparation and Stability of Nano-Scaled Gel Beads of λ-Carrageenan Bound with Ferric Ions. *Int. J. Biol. Macromol.* **2018**, *120*, 2523–2529. https://doi.org/10.1016/j.ijbiomac.2018.09.024.

(44) Characterization and Digestion Features of a Novel Polysaccharide-Fe(III) Complex as an Iron Supplement. *Carbohydr. Polym.* **2020**, *249*, 116812. https://doi.org/10.1016/j.carbpol.2020.116812.

(45) Groult, H.; Carregal-Romero, S.; Castejón, D.; Azkargorta, M.; Miguel-Coello, A.-B.; Reddy Pulagam, K.; Gómez-Vallejo, V.; Cousin, R.; Muñoz-Caffarel, M.; H. Lawrie, C.; Llop, J.; Piot, J.-M.; Elortza, F.; Maugard, T.; Ruiz-Cabello, J.; Fruitier-Arnaudin, I. Heparin Length in the Coating of Extremely Small Iron Oxide Nanoparticles Regulates in Vivo Theranostic Applications. *Nanoscale* **2021**, *13* (2), 842–861. https://doi.org/10.1039/D0NR06378A.

(46) Groult, H.; Poupard, N.; Herranz, F.; Conforto, E.; Bridiau, N.; Sannier, F.; Bordenave, S.; Piot, J.-M.; Ruiz-Cabello, J.; Fruitier-Arnaudin, I.; Maugard, T. Family of Bioactive Heparin-Coated Iron Oxide Nanoparticles with Positive Contrast in Magnetic Resonance Imaging for Specific Biomedical Applications. *Biomacromolecules* **2017**, *18* (10), 3156–3167. https://doi.org/10.1021/acs.biomac.7b00797.

(47) Zhang, A.; Meng, K.; Liu, Y.; Pan, Y.; Qu, W.; Chen, D.; Xie, S. Absorption, Distribution, Metabolism, and Excretion of Nanocarriers *in Vivo* and Their Influences. *Adv. Colloid Interface Sci.* **2020**, *284*, 102261. https://doi.org/10.1016/j.cis.2020.102261.

(48) Heurtault, B.; Saulnier, P.; Pech, B.; Proust, J.-E.; Benoit, J.-P. Physico-Chemical Stability of Colloidal Lipid Particles. *Biomaterials* **2003**, *24* (23), 4283–4300. https://doi.org/10.1016/S0142-9612(03)00331-4.

(49) Jynge, P.; Skjold, A. M.; Falkmer, U.; Andersson, R. G. G.; Seland, J. G.; Bruvold, M.; Blomlie, V.; Eidsaunet, W.; Karlsson, J. O. G. MnDPDP: Contrast Agent for Imaging and Protection of Viable Tissue. *Contrast Media Mol. Imaging* **2020**, *2020* (1), 3262835. https://doi.org/10.1155/2020/3262835.

(50) Diodati, S.; Pandolfo, L.; Caneschi, A.; Gialanella, S.; Gross, S. Green and Low Temperature Synthesis of Nanocrystalline Transition Metal Ferrites by Simple Wet Chemistry Routes. *Nano Res.* **2014**, *7* (7), 1027–1042. https://doi.org/10.1007/s12274-014-0466-3.

(51) Kambale, R. C.; Song, K. M.; Hur, N. Dielectric and Magnetoelectric Properties of BaTiO3–CoMn0.2Fe1.8O4 Particulate (0-3) Multiferroic Composites. *Curr. Appl. Phys.* **2013**, *13* (3), 562–566. https://doi.org/10.1016/j.cap.2012.10.007.

(52) Jain, R.; Gulati, S. Influence of Fe2+ Substitution on FTIR and Raman Spectra of Mn Ferrite Nanoparticles. *Vib. Spectrosc.* **2023**, *126*, 103540. https://doi.org/10.1016/j.vibspec.2023.103540.

(53) Testa-Anta, M.; Ramos-Docampo, M. A.; Comesaña-Hermo, M.; Rivas-Murias, B.; Salgueiriño, V. Raman Spectroscopy to Unravel the Magnetic Properties of Iron Oxide

Nanocrystals for Bio-Related Applications. *Nanoscale Adv.* **2019**, *1* (6), 2086–2103. https://doi.org/10.1039/C9NA00064J.

(54) Otero-Lorenzo, R.; Fantechi, E.; Sangregorio, C.; Salgueiriño, V. Solvothermally Driven Mn Doping and Clustering of Iron Oxide Nanoparticles for Heat Delivery Applications. *Chem. Weinh. Bergstr. Ger.* **2016**, *22* (19), 6666–6675. https://doi.org/10.1002/chem.201505049.

(55) *Solvothermal Clustering of Magnetic Spinel Ferrite Nanocrystals: A Raman Perspective | Chemistry of Materials*. https://pubs.acs.org/doi/10.1021/acs.chemmater.7b02881 (accessed 2024-04-12).

(56) *IJMS | Free Full-Text | Chondroitin-Sulfate-A-Coated Magnetite Nanoparticles: Synthesis, Characterization and Testing to Predict Their Colloidal Behavior in Biological Milieu*. https://www.mdpi.com/1422-0067/20/17/4096 (accessed 2024-04-12).

(57) You, S.-M.; Park, J.-S.; Luo, K.; Jeong, K.-B.; Adra, H. J.; Kim, Y.-R. Modulation of the Peroxidase-like Activity of Iron Oxide Nanoparticles by Surface Functionalization with Polysaccharides and Its Application for the Detection of Glutathione. *Carbohydr. Polym.* **2021**, *267*, 118164. https://doi.org/10.1016/j.carbpol.2021.118164.

(58) Liu, P.; He, H.; Wei, G.; Liang, X.; Qi, F.; Tan, F.; Tan, W.; Zhu, J.; Zhu, R. Effect of Mn Substitution on the Promoted Formaldehyde Oxidation over Spinel Ferrite: Catalyst Characterization, Performance and Reaction Mechanism. *Appl. Catal. B Environ.* **2016**, *182*, 476–484. https://doi.org/10.1016/j.apcatb.2015.09.055.

(59) Kim, K. J.; Lee, H. J.; Park, J. Y. Cationic Behavior and the Related Magnetic and Magnetotransport Properties of Manganese Ferrite Thin Films. *J. Magn. Magn. Mater.* **2009**, *321* (22), 3706–3711. https://doi.org/10.1016/j.jmmm.2009.07.021.

(60) Freire, R. M.; Ribeiro, T. S.; Vasconcelos, I. F.; Denardin, J. C.; Barros, E. B.; Mele, G.; Carbone, L.; Mazzetto, S. E.; Fechine, P. B. A. MZnFe2O4 (M = Ni, Mn) Cubic Superparamagnetic Nanoparticles Obtained by Hydrothermal Synthesis. *J. Nanoparticle Res.* **2013**, *15* (5), 1616. https://doi.org/10.1007/s11051-013-1616-3.

(61) El-Shater, R. E.; El Shimy, H.; Saafan, S. A.; Darwish, M. A.; Zhou, D.; Trukhanov, A. V.; Trukhanov, S. V.; Fakhry, F. Synthesis, Characterization, and Magnetic Properties of Mn Nanoferrites. *J. Alloys Compd.* **2022**, *928*, 166954. https://doi.org/10.1016/j.jallcom.2022.166954.

(62) Guo, J.; Zhu, S.; Chen, P.; Liu, Z.; Lin, L.; Zhang, J. Effect of Physiological pH on the Molecular Characteristics, Rheological Behavior, and Molecular Dynamics of κ-Carrageenan/Casein. *Front. Nutr.* **2023**, *10*, 1174888. https://doi.org/10.3389/fnut.2023.1174888.

(63) *Adsorption and Unfolding of a Single Protein Triggers Nanoparticle Aggregation | ACS Nano*. https://pubs.acs.org/doi/full/10.1021/acsnano.5b06439 (accessed 2023-06-12).

(64) Alford, J. K.; Rutt, B. K.; Scholl, T. J.; Handler, W. B.; Chronik, B. A. Delta Relaxation Enhanced MR: Improving Activation-Specificity of Molecular Probes through R Dispersion Imaging. *Magn. Reson. Med.* **2009**, *61* (4), 796–802. https://doi.org/10.1002/mrm.21933.

(65) Wendland, M. F. Applications of Manganese-Enhanced Magnetic Resonance Imaging (MEMRI) to Imaging of the Heart. *NMR Biomed.* **2004**, *17* (8), 581–594. https://doi.org/10.1002/nbm.943.

(66) *Carrageenan as a Potential Factor of Inflammatory Bowel Diseases*. https://www.mdpi.com/2072-6643/16/9/1367 (accessed 2025-01-27).

(67) Lopes, A. H.; Silva, R. L.; Fonseca, M. D.; Gomes, F. I.; Maganin, A. G.; Ribeiro, L. S.; Marques, L. M. M.; Cunha, F. Q.; Alves-Filho, J. C.; Zamboni, D. S.; Lopes, N. P.; Franklin, B. S.; Gombault, A.; Ramalho, F. S.; Quesniaux, V. F. J.; Couillin, I.; Ryffel, B.; Cunha, T. M. Molecular Basis of Carrageenan-Induced Cytokines Production in Macrophages. *Cell Commun. Signal.* **2020**, *18* (1), 141. https://doi.org/10.1186/s12964-020-00621-x.

(68) Tsuji, R. F.; Hoshino, K.; Noro, Y.; Tsuji, N. M.; Kurokawa, T.; Masuda, T.; Akira, S.; Nowak, B. Suppression of Allergic Reaction by λ-Carrageenan: Toll-like Receptor 4/MyD88-Dependent and -Independent Modulation of Immunity. *Clin. Exp. Allergy* **2003**, *33* (2), 249–258. https://doi.org/10.1046/j.1365-2222.2003.01575.x.

(69) Chen, H.; Wang, F.; Mao, H.; Yan, X. Degraded λ-Carrageenan Activates NF-κB and AP-1 Pathways in Macrophages and Enhances LPS-Induced TNF-α Secretion through AP-1. *Biochim. Biophys. Acta BBA - Gen. Subj.* **2014**, *1840* (7), 2162–2170. https://doi.org/10.1016/j.bbagen.2014.03.011.

(70) Kim, S.-K. *Marine Glycobiology: Principles and Applications*; CRC Press, 2016.

(71) Groult, H.; Cousin, R.; Chot-Plassot, C.; Maura, M.; Bridiau, N.; Piot, J.-M.; Maugard, T.; Fruitier-Arnaudin, I. λ-Carrageenan Oligosaccharides of Distinct Anti-Heparanase and

Anticoagulant Activities Inhibit MDA-MB-231 Breast Cancer Cell Migration. *Mar. Drugs* **2019**, *17* (3), 140. https://doi.org/10.3390/md17030140.

(72) *Numerical learning of deep features from drug-exposed cell images to calculate IC50 without staining | Scientific Reports*. https://www.nature.com/articles/s41598-022-10643-9 (accessed 2025-01-27).

(73) *Nanotoxicity of Silver Nanoparticles on HEK293T Cells: A Combined Study Using Biomechanical and Biological Techniques | ACS Omega*. https://pubs.acs.org/doi/10.1021/acsomega.8b00608 (accessed 2025-01-27).

(74) *Optimization of cell viability assays to improve replicability and reproducibility of cancer drug sensitivity screens | Scientific Reports*. https://www.nature.com/articles/s41598-020-62848-5 (accessed 2024-05-03).

(75) *Manganese-Enhanced T1 Mapping in the Myocardium of Normal and Infarcted Hearts - PubMed*. https://pubmed.ncbi.nlm.nih.gov/30498403/ (accessed 2024-06-25).

(76) *Manganese-enhanced T1 mapping to quantify myocardial viability: validation with 18F-fluorodeoxyglucose positron emission tomography | Scientific Reports*. https://www.nature.com/articles/s41598-020-58716-x (accessed 2024-06-25).

(77) Jasmin, N. H.; Thin, M. Z.; Johnson, R. D.; Jackson, L. H.; Roberts, T. A.; David, A. L.; Lythgoe, M. F.; Yang, P. C.; Davidson, S. M.; Camelliti, P.; Stuckey, D. J. Myocardial Viability Imaging Using Manganese-Enhanced MRI in the First Hours after Myocardial Infarction. *Adv. Sci.* **2021**, *8* (11), 2003987. https://doi.org/10.1002/advs.202003987.

(78) Spath, N. B.; Thompson, G.; Baker, A. H.; Dweck, M. R.; Newby, D. E.; Semple, S. I. K. Manganese-Enhanced MRI of the Myocardium. *Heart Br. Card. Soc.* **2019**, *105* (22), 1695–1700. https://doi.org/10.1136/heartjnl-2019-315227.

(79) Pan, D.; Caruthers, S. D.; Senpan, A.; Schmieder, A. H.; Wickline, S. A.; Lanza, G. M. Revisiting an Old Friend: Manganese-Based MRI Contrast Agents. *Wiley Interdiscip. Rev. Nanomed. Nanobiotechnol.* **2011**, *3* (2), 162–173. https://doi.org/10.1002/wnan.116.

(80) Ni, Y.; Petré, C.; Bosmans, H.; Miao, Y.; Grant, D.; Baert, A. L.; Marchal, G. Comparison of Manganese Biodistribution and MR Contrast Enhancement in Rats after Intravenous Injection of MnDPDP and MnCl2. *Acta Radiol. Stockh. Swed. 1987* **1997**, *38* (4 Pt 2), 700–707. https://doi.org/10.1080/02841859709172402.

(81) Leal, M. P.; Rivera-Fernández, S.; Franco, J. M.; Pozo, D.; Fuente, J. M. de la; García-Martín, M. L. Long-Circulating PEGylated Manganese Ferrite Nanoparticles for MRI-Based Molecular Imaging. *Nanoscale* **2015**, *7* (5), 2050–2059. https://doi.org/10.1039/C4NR05781C.

(82) *Manganese-based MRI contrast agents: past, present, and future - ScienceDirect*. https://www.sciencedirect.com/science/article/abs/pii/S0040402011011409 (accessed 2024-06-25).

TABLE OF CONTENTS GRAPHIC

For Table of Contents Use Only

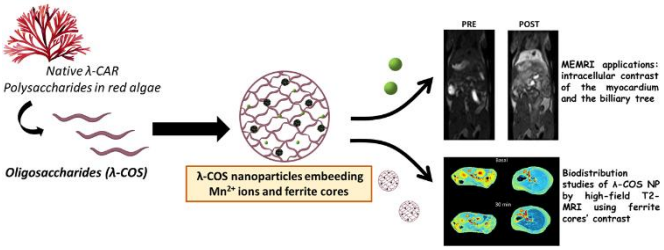
Native λ-CAR
Polysaccharides in red algae
Oligosaccharides (λ-COS)
λ-COS nanoparticles embeeding
Mn2+ ions and ferrite cores
PRE
POST
MEMRI applications: intracellular contrast of the myocardium and the billiary tree
Biodistribution studies of λ-COS NP by high-field T2-MRI using ferrite cores' contrast